

1 **Neural circuit mechanisms for transforming learned olfactory valences into wind-**
2 **oriented movement**

3 Yoshinori Aso^{1*}, Daichi Yamada², Daniel Bushey¹, Karen Hibbard¹, Megan Sammons¹,
4 Hideo Otsuna¹, Yichun Shuai¹, Toshihide Hige^{2,3,4*}

5 1: Janelia Research Campus, Howard Hughes Medical Institute, Ashburn, United States

6 2: Department of Biology, University of North Carolina at Chapel Hill, Chapel Hill, United
7 States

8 3: Department of Cell Biology and Physiology, University of North Carolina at Chapel Hill,
9 Chapel Hill, United States

10 4: Integrative Program for Biological and Genome Sciences, University of North Carolina
11 at Chapel Hill, Chapel Hill, United States

12

13 Contact Info

14 asoy@janelia.hhmi.org

15 hige@email.unc.edu

16

17 **Summary**

18 How memories are used by the brain to guide future action is poorly understood. In
19 olfactory associative learning in *Drosophila*, multiple compartments of the mushroom
20 body act in parallel to assign a valence to a stimulus. Here, we show that appetitive
21 memories stored in different compartments induce different levels of upwind locomotion.
22 Using a photoactivation screen of a new collection of split-GAL4 drivers and EM
23 connectomics, we identified a cluster of neurons postsynaptic to the mushroom body
24 output neurons (MBONs) that can trigger robust upwind steering. These UpWind
25 Neurons (UpWiNs) integrate inhibitory and excitatory synaptic inputs from MBONs of
26 appetitive and aversive memory compartments, respectively. After formation of
27 appetitive memory, UpWiNs acquire enhanced response to reward-predicting odors as
28 the response of the inhibitory presynaptic MBON undergoes depression. Blocking
29 UpWiNs impaired appetitive memory and reduced upwind locomotion during retrieval.
30 Photoactivation of UpWiNs also increased the chance of returning to a location where
31 activation was terminated, suggesting an additional role in olfactory navigation. Thus,
32 our results provide insight into how learned abstract valences are gradually transformed
33 into concrete memory-driven actions through divergent and convergent networks, a
34 neuronal architecture that is commonly found in the vertebrate and invertebrate brains.

35

36 **Introduction**

37 Animals assign a valence to a stimulus based on experience. Such learning events
38 induce an enduring modification in the stimulus-evoked activity of the nervous system
39 and ultimately change the behavioral response to future encounters with the same
40 stimulus. In mammals, the amygdala is the primary site for valence assignment during
41 Pavlovian learning (O'Neill et al., 2018). As a neutral sensory stimulus (conditioned
42 stimulus, CS) is paired with punishment or reward (unconditioned stimulus, US), the CS

43 acquires the capacity to evoke valence-specific response patterns in the amygdala
44 (Grewe et al., 2017; Zhang and Li, 2018). However, the circuit process in which these
45 learning-dependent CS representations lead to concrete motor patterns during memory
46 retrieval is poorly understood. Comprehensive understanding of this process requires
47 detailed knowledge of the downstream connectivity of the plastic CS-representing
48 neurons. Nevertheless, it has been shown that amygdala-dependent valence-specific
49 behaviors are mediated by distinct networks (Gore et al., 2015) whose outputs diverge to
50 different projection areas responsible for aversive or appetitive unconditioned responses
51 (Beyeler et al., 2016; Namburi et al., 2015). There is also evidence for an alternative
52 mechanism where neurons capable of eliciting opposing behaviors converge on the
53 same target areas or neurons. For example, GABAergic and glutamatergic projection
54 neurons from the lateral hypothalamus to the ventral tegmental areas (VTA) can evoke
55 appetitive and aversive behaviors, respectively. These projection neurons converge on
56 the same population of GABAergic neurons in VTA to differentially control downstream
57 dopaminergic neurons (Nieh et al., 2016). Thus, both divergent and convergent circuit
58 motifs are considered important for the valence-to-behavior transformation in vertebrates
59 (Tye, 2018).

60

61 Divergent pathways for valence processing are also evident in the memory circuit in
62 *Drosophila* both anatomically and functionally. In fly olfactory learning, the primary site
63 for CS-US association is the mushroom body (MB), where parallel axon fibers of the
64 odor-encoding Kenyon cells (KCs) are segmented into a series of MB compartments that
65 are defined by the dendrites of MB output neurons (MBONs) and axons of US-encoding
66 dopaminergic neurons (DANs) (Aso et al., 2014a; Tanaka et al., 2008)(Figure 1A). While
67 population activity of KCs represents odor identity (Campbell et al., 2013), that of
68 MBONs is less effective in doing so (Hige et al., 2015b). Instead, individual MBONs are

69 considered to encode the valence of stimuli because optogenetic activation of each type
70 of MBONs can elicit either approach or avoidance behavior (Aso et al., 2014b; Owald et
71 al., 2015). However, MBONs do not appear to command specific motor sequences
72 because their activation does not induce stereotyped motor patterns (Aso et al., 2014b).
73 Thus, how abstract valence signals carried by MBONs are translated into concrete motor
74 patterns is unknown.

75

76 The MB compartments are arranged such that the valence of DANs is opposite to that of
77 the corresponding MBONs in a given compartment (Aso et al., 2014b). During learning,
78 coactivation of DANs and KCs induces long-term depression of KC-MBON synapses in
79 a compartment-specific manner (Berry et al., 2018; Cohn et al., 2015; Hige et al., 2015a;
80 Owald et al., 2015). Thus, the prevailing hypothesis is that learning-induced depression
81 in a subset of MBONs tips the collective balance of positive and negative valences
82 represented by the MBON population, which are in balance in naive flies, and thereby
83 biases the odor choice (Heisenberg, 2003; Hige, 2018; Modi et al., 2020; Owald and
84 Waddell, 2015). Supporting this view, photoactivation of multiple types of MBONs
85 encoding the same or opposite valences exerts additive effects for induction of attraction
86 and avoidance (Aso et al., 2014b). This model predicts that the circuits downstream of
87 the MB should be sensitive to skewed activity patterns of the MBON population. Such a
88 computation can be performed by neurons integrating or comparing the output signals of
89 multiple MBONs. In fact, axon terminals of the MBONs are confined to relatively limited
90 brain regions, suggesting that they converge on common neurons (Aso et al., 2014a).
91 The comprehensive EM connectome indeed revealed that 600 out of 1550 postsynaptic
92 neurons of MBONs also receive input from at least one other MBON (Li et al., 2020).
93 However, whether those convergent circuit motifs function to decode the parallel

94 memories formed in the MB and, if so, how they shape motor patterns during memory
95 retrieval are unknown.

96

97 The functional diversity of the MB compartments is not limited to the sign of memory
98 valence. At least 5 out of 15 MB compartments are identified as appetitive memory
99 compartments, and yet they exhibit distinct memory properties (Aso et al., 2014b; Aso
100 and Rubin, 2016). For example, memory formation in the $\alpha 1$ compartment requires
101 relatively long training, but once formed, lasts more than a day. In contrast, memory in
102 $\gamma 5\beta'2\alpha$ requires only a single training to form but is transient and easily overwritten by
103 the subsequent training (Aso and Rubin, 2016; Ichinose et al., 2021; Yamada et al.,
104 2023). Compartments are also tuned to distinct types of reward. While $\alpha 1$ memory is
105 essential for nutritional value learning (Yamagata et al., 2015), $\gamma 4$ and $\beta'2$ compartments
106 function in water reward learning (Lin et al., 2014). Despite this diversity, memory
107 formation in any appetitive compartments can promote attraction to the associated odor.
108 However, the behavioral strategies used to find the source of attractive odors are not
109 analyzed in typical olfactory learning assays using T-maze (Tully and Quinn, 1985),
110 which only measure the relative distributions of flies between learned and control odors.
111 Thus, the roles played by individual appetitive memory compartments in guiding
112 approach to an attractive odor remain unknown.

113

114 By analyzing walking trajectories of individual flies, we found that appetitive memories
115 formed in the $\alpha 1$ compartment are able to bias the turning direction so that flies move
116 upwind. By photoactivation screening, we identified a single cluster of neurons, UpWiNs,
117 that can promote robust upwind steering and acceleration of locomotion. UpWiNs
118 receive inputs from several types of lateral horn neurons and integrate inhibitory and
119 excitatory inputs from MBON- $\alpha 1$ and MBON- $\alpha 3$, which are the output neurons of MB

120 compartments that store long-lasting appetitive or aversive memories, respectively (Aso
121 and Rubin, 2016; Ichinose et al., 2015; Jacob and Waddell, 2022a; Pai et al., 2013;
122 Yamagata et al., 2015). UpWiNs enhance responses to odors after induction of memory
123 in the α 1, and the activity of UpWiNs is required for appetitive memory and memory-
124 driven upwind locomotion. Taken together, our work provides important insights into the
125 process of valence integration, which we show employs a convergent circuit motif
126 commonly found downstream of memory centers, and reveals circuit mechanisms that
127 underlie the gradual transformation from abstract valence to specific motor commands.

128

129 **Results**

130 **Identification of the MB compartments that drive upwind locomotion**

131 To analyze behavioral components of memory-driven odor response, we used a
132 modified four-armed olfactory arena in which odors are delivered through the current of
133 airflow from the four channels at corners to the suction tubing at the center (Figure 1B)
134 (Aso and Rubin, 2016; Pettersson, 1970; Vet et al., 1983). The airstream from each
135 channel forms sharp boundaries at the border of quadrants. Each of four quadrants can
136 be filled with an arbitrary odor, but we typically used it either for presentation of a single
137 odor in all quadrants or for binary choice by presenting two odors in diagonal quadrants
138 (Figure 1C). Olfactory memories can be assessed by binary choice between two odors
139 or by analyzing kinematic parameters and wind-directional behaviors in the presence of
140 learned odor. When flies were repeatedly trained by pairing one of two odors with
141 optogenetic activation of sugar sensory neurons, flies gradually increased upwind
142 locomotion in response to the paired odor but developed odor preference in the binary
143 choice more rapidly (Figure 1D-E). As a result, the learning rate measured by odor
144 preference was much faster than that measured by upwind locomotion (Figure 1F). This
145 observation and distinct dynamics of memory and plasticity in the MB lobes and

146 compartments (Aso et al., 2012; Aso and Rubin, 2016; Hige et al., 2015a; Huettneroth et
147 al., 2015; Ichinose et al., 2021, 2015; Jacob and Waddell, 2022a; Pai et al., 2013;
148 Pascual and Prétat, 2001; Plaçais et al., 2013; Séjourné et al., 2011; Vrontou et al.,
149 2021; Yamagata et al., 2015; Zars et al., 2000) led us to hypothesize that appetitive
150 olfactory memories created in different MB compartments elicit distinct behaviors during
151 memory retrieval.

152 To test the hypothesis, we first trained flies by pairing an odor as the CS+ with
153 optogenetic activation of one of four sets of DANs. Each set of DANs projects to distinct
154 appetitive memory compartments: γ 5 β '2a, γ 4, β 1 β 2 or α 1 (Huettneroth et al., 2015;
155 Ichinose et al., 2015; Lin et al., 2014; Liu et al., 2012; Yamagata et al., 2015). A second
156 odor was presented without DAN activation as CS- (Figures 1G). These optogenetic
157 activations promoted local release of dopamine in the targeted MB compartments (Sun
158 et al., 2020; Yamada et al., 2023). We used a pair of odors, Pentyl Acetate (PA) and
159 Ethyl Lactate (EL), that evokes activity in discrete sets of KCs (Campbell et al., 2013).
160 After three training sessions, flies exhibited strong preference to the CS+ odor when
161 given a choice between CS+ and CS- odors (Figure 1H). Next, we asked if these MB-
162 compartment-specific memories can drive wind-directed movement when CS+ or CS-
163 odors were presented separately for 10 seconds (Figure 1G). We measured the
164 movement of individual flies and their heading angle relative to the upwind direction and
165 analyzed how those parameters changed in response to odors. Despite robust CS+
166 preference in a binary choice, memories in the γ 5 β '2a and the γ 4 failed to promote
167 significant upwind movement (Figure 1I-J). In contrast, memories in the α 1 and the β 1 β 2
168 promoted steering and walking upwind in response to the CS+ odor, compared to
169 genetic controls and the “No LED” control group of the same genotype (Figure 1I-J). The
170 memory in the α 1 compartment also reduced upwind locomotion in response to CS-
171 odor compared to the genetic control groups. These initial analyses compared averages

172 of all ~20 flies in each movie. By separately analyzing behaviors of individual flies based
173 on their orientation at the onset of odors, we found that memories in the α 1 and β 1 β 2
174 biased the direction of turning to steer toward upwind (Figure 1 K-L). Memories in γ 5 β '2a
175 and γ 4 did not bias the turning direction, although they promoted flies initially facing
176 downwind to change orientation in a non-directional manner (Figure 1K-L and Figure 1-
177 figure supplement 1) and flies tended to orient toward upwind during CS+ odor
178 presentation (Figure 1I). These results indicate that appetitive memory retrieval involves
179 distinct behavioral strategies depending on the localization of the memory in the MB.
180 Specifically, we expected that MBONs from the α 1 and the β 1 β 2 compartments are
181 preferentially connected to circuit components that drive memory-driven upwind steering.

182

183 **Identification of UpWind Neurons by optogenetic screening**

184 We next set out to identify the circuit elements that function downstream of the MBONs
185 to induce memory-driven, wind-guided locomotion. To enable cell-type-specific
186 experimental manipulation, we have made a large collection of split-GAL4 drivers (Shuai
187 et al., 2023). Using a subset of these lines, we conducted optogenetic screening to test if
188 activation of certain neurons can promote wind-directed movement. We analyzed how
189 starved flies respond to 10-s optogenetic stimulation of various cell types in the circular
190 arena with airflow but no olfactory stimuli (Figure 2). We measured the changes in the
191 fly's distance from the center, heading angle relative to the upwind direction, angular
192 velocity and walking speed. Because returning to the odor plume is a major component
193 of olfactory navigation (Baker, 1990; Cardé, 2021), we also measured the probability of a
194 fly returning to its starting location after moving away.

195 Although our screen is not comprehensive in terms of the coverage of the cell
196 types or brain areas, it successfully identified several clear “hits”, which include both
197 known and previously uncharacterized cell types. Four lines, which label SMP120/124,

198 MBON01/03/04 or CRE039, promoted locomotion in the downwind direction (Figure 2
199 and Figure 2-figure supplement 1 and 2). As previously reported (Matheson et al., 2022),
200 activation of some MBON types including MBON- α 3 (also known as MBON14 or MBON-
201 V3) and MBON- γ 2 α' 1 (MBON12) promoted significant upwind locomotion. Figure 2B
202 summarizes the detailed time courses of these behavioral phenotypes before, during
203 and after 10-s LED stimulations. These behavioral data can be immediately put into the
204 context of the EM connectome map, since the cell types in each driver lines were
205 morphologically matched by comparing confocal and electron microscope images (see
206 examples in Figure 2-figure supplement 3 and 4).

207 Among the split-GAL4 drivers we screened, SS33917 and SS33918 showed the
208 strongest upwind locomotion, especially at the onset of 10-s activation period (Video 1
209 and 2; Figure 2B and Figure 2-figure supplement 1). These driver lines label a similar set
210 of 8-11 neurons (Figure 2-figure supplement 2). Here, we will focus our analysis on this
211 cluster of neurons, which we collectively call UpWind Neurons (UpWiNs), based on their
212 robust activation phenotype and anatomical connections with the α 1 compartment (see
213 below).

214

215 **UpWiNs integrate inputs from MBONs**

216 The UpWiNs have extensive arborizations in the posterior dorsolateral area of the brain
217 where MBON- α 1 (also known as MBON07) and MBON- α 3 (also known as MBON14)
218 send converging axons (Video 3; Figure 3A). DANs innervating the α 1 and α 3
219 compartments respond to sugar or electric shock/heat/bitter, and activation of DANs can
220 substitute US to induce long-lasting appetitive and aversive memories, respectively (Aso
221 and Rubin, 2016; Huettneroth et al., 2015; Ichinose et al., 2015; Jacob and Waddell,
222 2022b; Kirkhart and Scott, 2015; Matheson et al., 2022; Pai et al., 2013; Schnitzer et al.,
223 n.d.; Siju et al., 2020; Vrontou et al., 2021; Yamagata et al., 2015). MBON- α 1 displays

224 reduced odor response to an odor associated with activation of DANs in α 1 (Yamada et
225 al., 2023), whereas MBON- α 3 increases response to an odor associated with sugar
226 reward possibly due to interactions with appetitive memory compartments such as the
227 β 1 (Li et al., 2020; Plaçais et al., 2013; Takemura et al., 2017; Tanaka et al., 2008) and
228 decreases response to punishment-associated odors (Jacob and Waddell, 2022a;
229 Schnitzer et al., n.d.). Both MBONs are required for retrieval of long-term appetitive
230 memory (Ichinose et al., 2015; Plaçais et al., 2013). These previous reports raise the
231 possibility that the UpWiNs defined by the SS33917 driver might play a role in both the
232 upwind locomotion observed during retrieval of an α 1 memory (Figure 1) and the
233 activation of MBON- α 3 (Matheson et al., 2022)(MB082C data in Figure 2).

234 To test this possibility, we first examined the anatomical connectivity of the
235 UpWiNs. We obtained images of 25 individual neurons in SS33917-split-GAL4 by the
236 multi-color flip-out method and compared them with reconstructed EM-images (Figure 3
237 and Figure 3 supplement 1-3) (Nern et al., 2015; Otsuna et al., n.d.; Scheffer et al.,
238 2020). This analysis identified eleven neurons of five cell types in the hemibrain EM
239 dataset that resemble UpWiNs in SS33197 driver (Figure 3 Figure supplement 1 and 2).
240 Among 11 matched EM-reconstructed neurons of the UpWiNs, four neurons, one
241 SMP353 and three SMP354 neurons, receive direct synaptic input from MBON- α 1
242 (Figure 3B-E)(Li et al., 2020; Scheffer et al., 2020). SMP354 also receives input from
243 MBON- α 3; this strong convergent connectivity is exceptional among the population of
244 the neurons that are postsynaptic to either of the MBONs (Figure 3D-E and Figure 3-
245 figure supplement 4). The rest of the UpWiNs do not have direct connections with these
246 MBONs but receive indirect input from them via connections among UpWiNs (Figure
247 3F). The interconnection within the UpWiN cluster suggests that these neurons may
248 function as a group, even though the connectivity of the individual neurons is
249 heterogeneous. Interestingly, all the UpWiNs provide input to a single neuron, SMP108

250 (Figure 3C), which has the highest number of connections with reward DANs and plays
251 a key role in second-order conditioning (Yamada et al., 2023). The axon terminals of
252 UpWiNs are immunoreactive to choline acetyltransferase (Yamada et al., 2023), and
253 therefore likely to be excitatory to the SMP108 and other downstream neurons. The
254 SMP108 is labeled in SS45234 and SS67221, and its activation also promoted upwind
255 locomotion (Figure 2; Figure 2-figure supplement 1).

256

257 To test functional connectivity, we made *in vivo* whole-cell recordings from
258 UpWiNs while optogenetically activating either MBON- α 3 or MBON- α 1. Neurons were
259 randomly targeted by the electrode among those labeled by R64A11-LexA, which is a
260 broad driver for UpWiNs. R64A11 is a hemi-driver for the DNA-binding domain of the
261 SS33917-split-GAL4. A brief 10-ms stimulation of cholinergic MBON- α 3 evoked a strong
262 excitation in 3 out of 11 UpWiNs examined, whereas glutamatergic MBON- α 1 evoked
263 inhibitory responses in 4 out of 17 UpWiNs (Figure 4A-B). The observed stochasticity of
264 the connectivity is consistent with the EM connectome data.

265

266 Postsynaptic sites of MBON- α 1 and MBON- α 3 are juxtaposed on the dendrites of
267 UpWiNs (Figure 3E), implying dendritic integration of these inputs. Since we did not
268 have a LexA driver that selectively labels SMP354, we were unable to specifically target
269 those integrating UpWiNs by electrophysiology. We therefore measured the population
270 activity of UpWiNs at the junction between their dendrites and proximal axons by two-
271 photon calcium imaging in dissected brains. Consistent with the electrophysiological
272 results and the circuit model, we observed a calcium increase upon MBON- α 3 activation.
273 Moreover, MBON- α 1 activation suppressed the excitatory effect of MBON- α 3 when they
274 were activated together (Figure 4C).

275

276 Finally, we tested the presence of excitatory interconnection between UpWiNs.
277 We expressed GCaMP6s in a broad population of UpWiNs using 64A11-LexA while
278 expressing Chrimson-tdTomato in a small subset using SS67249 split-GAL4. The flies
279 also carried UAS-LexAp65-DBD2-RNAi to suppress the expression of GCaMP in
280 Chrimson-positive UpWiNs (Figure 4 – figure supplement 1 A-B). 1-s photostimulation
281 evoked excitatory GCaMP response both in axons and dendrites (Figure 4 – figure
282 supplement 1C). These results indicate that as a population, UpWiNs receive and
283 integrate synaptic inputs from MBONs that signal opposite signs of memory valence.

284

285 **UpWiNs acquire enhanced responses to reward-predicting odors**

286 The UpWiN cluster collectively receives olfactory information from the MBONs and
287 lateral horn output neurons (Figure 3C). This anatomy raises the intriguing possibility
288 that UpWiNs have basal odor responses and that memories in the MB modify it. To test
289 this possibility, we optogenetically induced appetitive memory and monitored the change
290 in the subsequent odor-evoked electrophysiological activity of UpWiNs (Figure 5A). For
291 these experiments, we used another UpWiNs split-GAL4 driver SS67249. This driver
292 was not suitable for behavioral experiments due to stochastic and off-targeted
293 expression but labeled a highly restricted subset (1-3 cells) of UpWiNs including the one
294 resembling the morphology of SMP353 (Figure 5-figure supplement 1). Before training,
295 the UpWiNs showed relatively weak odor responses (Figure 5B) likely because inhibitory
296 and excitatory inputs cancel each other (Figure 4C). After pairing an odor with
297 optogenetic activation of reward DANs including those projecting to α 1, UpWiNs
298 displayed increased excitatory response to subsequent exposures to the CS+ odor but
299 not to the CS- odor (Figures 5B-D). We observed the enhancement of CS+ response
300 irrespective of the identity of tested CS+ odors (OCT or MCH; Figure 5-figure
301 supplement 2). This enhancement of CS+ response can be most easily explained as an

302 outcome of disinhibition from MBON- α 1 whose output had been decreased by memory
303 formation; MBON- α 1 is inhibitory to UpWiNs (Figure 4B) and MBON- α 1 response to the
304 CS+ is reduced following the same training protocol (Yamada et al., 2023). In addition to
305 such a mechanism, plasticity in the β 1 compartment may also contribute to the
306 enhanced CS+ response in UpWiNs because the driver R58E02-LexA contains DANs in
307 the β 1 and glutamatergic MBON from the β 1 directly synapse on the dendrites of
308 MBON- α 1 and MBON- α 3 (Takemura et al., 2017).

309

310 **UpWiNs promote wind-directed behaviors**

311 Having examined the functional connectivity and plasticity of UpWiNs, we revisited
312 behavioral phenotypes caused by optogenetic activation. In the screening experiments
313 shown in Figure 2, since the default wind direction is from the periphery to the center in
314 our olfactory arena, upon activation of UpWiNs, flies moved toward the periphery and
315 increased their mean distance from the center. However, this phenotype might be
316 explained by the avoidance of center area (Besson and Martin, 2005) rather than wind-
317 directed behavior. Several experiments argue against that possibility. First, the UpWiN
318 activation phenotype was starvation dependent; only starved flies showed robust upwind
319 locomotion upon UpWiN activation (Figure 6A). Second, flies' response to UpWiN
320 activation depended on the rate and direction of the airflow. Flies did not move toward
321 the periphery without airflow (Video 4) and moved toward the center when the direction
322 of airflow was reversed (Figure 6B). Finally, unilateral, or bilateral ablation of aristae, the
323 wind-sensing organ in Drosophila (Yorozu et al., 2009), impaired movement toward the
324 periphery during UpWiN activation (Figure 6C; Video 5). These observations are
325 consistent with a role for UpWiNs in transforming appetitive memory into wind-directed
326 behaviors.

327

328 As observed in memory-driven olfactory responses (Figure 1 and Figure 1-figure
329 supplement 1), the kinematics of behavior at the onset of UpWiN activation depended on
330 the initial orientation of flies relative to the wind-direction (Video 2). Flies transiently
331 increased angular speed during the first ~300 ms (Figure 6D). This increased angular
332 speed was observed also in empty-split-GAL4 control flies and considered to be a startle
333 response to activating light. However, direction of turning during this period was
334 significantly biased toward the upwind direction when either of two lines for UpWiNs
335 were used to express CsChrimson (Figure 6E-F). UpWiNs activation also modulated
336 forward walking speed in a manner that depended on the orientation of flies at the onset
337 of the activating light (Figure 6G). The orientation-dependent modulation of turning
338 direction and walking speed observed is similar to that evoked by α 1-specific memory
339 (Figure 1K). In contrast, activation of MBON- γ 2 α '1 with MB077B split-GAL4 modulated
340 forward walking speed and promoted flies that already faced upwind to maintain that
341 orientation but did not cause directional turning toward the upwind direction (Figure 6D-
342 G; see Figure 6-figure supplement 1 for other drivers). These results are consistent with
343 a view that UpWiNs transform memory in a α 1 into signals that promote olfactory
344 navigation but do not yet specify lower-level motor parameters (i.e. turning direction and
345 acceleration). Information about wind-direction and UpWiN's activity needs to be
346 integrated somewhere downstream to compute the turning direction. The central
347 complex is the likely brain area for such a computation (Matheson et al., 2022; Okubo et
348 al., 2020).

349

350 **UpWiNs are required for memory-driven upwind locomotion**

351 Finally, we asked if UpWiNs are required for retrieval of sugar-induced appetitive
352 memory. Formation of long-lasting appetitive memory after odor-sugar conditioning
353 relies on the DANs that innervate the α 1 compartment (Ichinose et al., 2021; Yamagata

354 et al., 2015). Therefore, we tested the requirement of UpWiNs for 1-day appetitive
355 memory. The control genotypes showed enhanced upwind locomotion in the presence of
356 odors associated with sugar, whereas flies that express the light chain of tetanus toxin
357 (TNT) in UpWiNs showed compromised upwind-locomotion (Figure 7A-B). To test the
358 requirement of UpWiNs specifically during the memory test period, we also attempted
359 experiments with temperature-sensitive *shibire*, which allows reversible block of
360 vesicular release (Kitamoto, 2001). One day after odor-sugar conditioning, blocking
361 synaptic output of UpWiNs only during test period impaired preference to CS+ odor in
362 binary choice compared to the genetic controls (Figure 7C). However, we were unable to
363 analyze wind-directional behaviors in these *shibire* experiments because control flies did
364 not show CS+ odor-induced upwind locomotion at restrictive temperature (data not
365 shown) presumably due to increased preference to the peripheral of the arena or altered
366 odor concentration. These results indicate that UpWiNs play a major role in behavior
367 during appetitive memory retrieval but also suggest that their behavioral contribution
368 may not be limited to simple promotion of upwind locomotion. Indeed, the analysis of 10-
369 s activation screening data revealed that flies increased the probability of revisiting the
370 location where UpWiNs activation was ended (Figure 2B). Although this data does not
371 necessarily indicate induction of spatial memory by UpWiNs, revisiting behavior cannot
372 be explained by a simple increase in turning probability. The return probability plotted in
373 Figure 7E is probability of return to the position at the end of LED period within 15-s
374 post-LED period when angular speed of SS33917>CsChrimson and
375 SS33918>CsChrimson flies are identical to empty-split-GAL4>CsChrimson control flies
376 (Figure 7-figure supplement 1). Another set of cell types SMP357-362 defined by
377 SS49755-split-GAL4 caused far more robust revisiting phenotype (Video 6; Figure 2B
378 and Figure 2-figure supplement 2). Finally, we found that optogenetic activation of the
379 UpWiNs could bias spatial distribution of flies between quadrants with and without

380 activating illumination (Figure 7D). This bias is likely due to the airflow-independent
381 function of UpWiNs because the UpWiN activation could increase the probability of
382 revisiting behavior even in the absence of airflow (Figure 7E and Figure 7-figure
383 supplement 1).

384

385 **Discussion**

386 It has been postulated that the valence of learned odors is represented as the relative
387 activity of the MBONs, each of which signals either positive or negative valence
388 assigned in the parallel memory modules. In this study, we identified a cluster of neurons
389 that can decode the differential activity of MBONs encoding opposing valances.
390 Although activity of these neurons strongly induced a coordinated sequence of motor
391 patterns that are deeply related to olfactory navigation, determination of turning direction
392 and walking speed depended on fly's orientation to wind direction. Thus, our findings
393 may mark an important transition point of the circuit, where abstract valence signals
394 encoded by a population of neurons are evaluated and gradually transformed into
395 concrete motor patterns.

396

397 **Memory valence and competing drives**

398 Previous studies in the Drosophila MB have predicted the existence of a valence
399 integration process. First, flies can create appetitive and aversive memories in parallel in
400 different MB compartments after a single learning experience, and those memories
401 compete over the behavioral choice with distinct time courses (Aso et al., 2014b; Aso and
402 Rubin, 2016; Das et al., 2014; Kaun et al., 2011). Second, memory extinction (Felsenberg
403 et al., 2018) and reversal learning (McCurdy et al., 2021) create a memory trace in a MB
404 compartment, which neutralizes the effect of the original memory traces that persist in other

405 MB compartments. Third, attraction and avoidance behaviors induced by photoactivation of
406 multiple types of MBONs can be largely explained by the additive effects of individual
407 activation (Aso et al., 2014b).

408

409 These studies support the “valence-balance model”, where learning-induced plasticity in
410 the MB tips the balance of the valence signals of the MBON population (Heisenberg, 2003;
411 Hige, 2018; Modi et al., 2020; Owald and Waddell, 2015). The mode of synaptic integration
412 observed in the UpWiNs matches the expectation from this model. UpWiNs receive direct
413 inhibitory and excitatory synaptic inputs from MBONs of appetitive and aversive memory
414 compartments, respectively. When both presynaptic MBONs were activated, which
415 mimicked the naive state (i.e. no depression in either of the MBONs), those inputs
416 canceled each other, resulting in no net excitation (Figure 4). When plasticity was induced
417 in the inhibitory appetitive-memory MBONs, which mimics appetitive memory formation, the
418 odor response was enhanced (Figure 5). Thus, UpWiNs are able to decode the unbalanced
419 activity of MBONs encoding opposing valence. Given the prevalence of convergent circuit
420 motifs in the downstream circuits of the MB (Li et al., 2020), we predict that similar synaptic
421 integration of those output neurons that signal the same or opposite stimulus valences
422 controls other components of olfactory behaviors. Convergence of valence signals might
423 also occur between the MB and LH, which is the other olfactory center parallel to the MB
424 and is thought to mediate innate behavior. In fact, one MBON type sends its axon to the LH
425 and causes learning-dependent modulation of the activity of food-odor-responding neurons
426 (Dolan et al., 2018). UpWiNs also receive abundant input from the LH neurons, suggesting
427 that UpWiNs also play an important role in integrating the innate and learned valances. The
428 use of divergent and convergent pathways to process valence signals, like those we

429 describe here, appear to be an evolutionarily conserved strategy that is observed, for
430 example, in the vertebrate amygdala and its associated brain areas (Tye, 2018).

431

432 **UpWiNs and olfactory navigation**

433 In addition to valence integration, UpWiNs play an important role in wind-guided behavior.
434 Wind direction provides a critical cue for olfactory navigation in natural environments where
435 odorants are propagated by the stream of airflow. Male moths have an astonishing ability to
436 track the source of attractant pheromones emitted from females located over a mile away,
437 and have been used as a model for olfactory navigation (Cardé, 2021; Kanzaki and Ikeda,
438 1994; Vergassola et al., 2007). Male moths react to the intermittent plume of pheromone by
439 series of cast-surge-cast actions (Baker, 1990). In a wind tunnel experiment, *Cadra*
440 *cautella* moths began cross-wind casting following withdrawal of the pheromone plume.
441 Upon contact with a single puff of pheromone, moths surged upwind after a delay of
442 approximately 200 ms to re-orient themselves. In our optogenetic experiments, activation of
443 UpWiNs increased angular velocity with a similar time scale and biased turning direction
444 toward the upwind direction (Figure 6D-F). In addition to promoting an upwind surge,
445 UpWiNs activation increased the probability of returning to the location where activation
446 was applied even after the cessation of both optogenetic activation and airflow (Figure 7
447 and Figure 7-figure supplement 1). Therefore, we speculate that UpWiNs alone may be
448 able to promote a series of cast-surge-cast reactions when flies navigate intermittent
449 plumes of reward-predicting odors. Furthermore, as the third function, UpWiNs can
450 promote release of dopamine in multiple MB compartments, presumably via converging
451 connection with SMP108 which in turn feeds excitatory inputs to multiple DANs to instruct
452 formation of second-order memories (Yamada et al., 2023). Interestingly, the patterns of

453 DAN population responses to SMP108 or UpWiNs activation are similar to those observed
454 when flies are walking toward vinegar in a virtual environment (Zolin et al., 2021). Together
455 with the evidence of inputs from the lateral horn neurons, this may indicate that UpWiNs is
456 also responsible for upwind locomotion to innately attractive odors and can be the causal
457 source of action correlates in DANs. All three of these UpWiNs functions likely contribute to
458 olfactory navigation in complex environments. Our study was limited to walking behaviors,
459 and the role of UpWiNs in flight behaviors remains to be investigated. UpWiNs are also
460 well-positioned to influence internal state to promote selective processing of wind and
461 olfactory stimuli.

462 Recent studies in *Drosophila* have provided insights into detailed neural circuit
463 mechanisms of wind sensation and olfactory navigation. Both flying and walking flies
464 turn upwind and increase locomotion speed when they encounter an attractive odor
465 (Álvarez-Salvado et al., 2018; Steck et al., 2012; van Breugel and Dickinson, 2014).
466 Airflow is detected by displacement of aristae and the Johnston organ sensory neurons
467 (Kamikouchi et al., 2006; Yorozu et al., 2009), and left-right asymmetry is computed by
468 the downstream neurons to represent wind direction in the central complex (Matheson et
469 al., 2022; Okubo et al., 2020; Suver et al., 2019). Fictive appetitive and aversive training
470 using optogenetic activation of DANs can promote and suppress the upwind locomotion,
471 respectively (Handler et al., 2019), suggesting that retrieval of associative memory to
472 drive behavior utilizes this same navigational strategy. Activation of a set of input
473 neurons of the fan-shaped body (FB), which is a part of the central complex known as
474 the navigation center of insects, can induce robust upwind locomotion (Matheson et al.,
475 2022). The FB is one of the major downstream targets of MBONs (Li et al., 2020;
476 Scaplen et al., 2021) while also receiving input from neurons representing wind
477 directions (Matheson et al., 2022). Although these studies point to the importance of the

478 central complex as the integration site of information about learned odor and wind
479 direction, much remains to be learned about how the valence signals conveyed by
480 MBONs influence upwind locomotion.

481 Based on the EM connectome data, SMP108 appears to be the most prominent
482 neuron postsynaptic to UpWiNs. Activation of SMP108 was able to promote upwind
483 locomotion, but the details of behavioral response differed from UpWiNs activation
484 (Figure 2), and blocking SMP108 did not affect retrieval of appetitive memory (Yamada
485 et al., 2023). Therefore, UpWiNs may evoke upwind behavior through other downstream
486 cells. FB6D, FB6I and FB6T appear to be other major downstream neurons of UpWiNs
487 (Figure 3C). The top 3 downstream neurons of FB6D are hDeltaF, hDeltaC and hDeltaK.
488 hDeltaC is the columnar cell type of the FB that is known to integrate wind-directional
489 cues and information of innately attractive odor to promote upwind behavior (Matheson
490 et al., 2022). Our screening also identified that co-activation of hDeltaB, hDeltaD and
491 hDeltaE can promote robust upwind locomotion (Figure 2 and Figure 2-figure
492 supplement 1 and 3). Thus these hDelta cell types likely function together to regulate
493 wind-directed locomotion. EM-connectome-guided follow-up studies on other cell types
494 with significant upwind/downwind phenotypes (Figure 2) will help generate a
495 comprehensive understanding of olfactory navigation circuits.

496

497 **Compartment-specific contribution to anemotaxis**

498 One highlight of our study is the finding that memories stored in different MB
499 compartments use different behavioral strategies during retrieval. Although gaining a full
500 description of those behavioral strategies is beyond the scope of the present study, we
501 can speculate on the potential biological significance of the differential contributions to
502 anemotaxis—movement in response to air currents—behaviors by MB compartments.

503 First, the difference in the type of memory stored in different compartments is likely
504 to be a key factor. Based on the circuit connectivity and behavioral data, UpWiNs are
505 responsible for upwind locomotion driven by the memory stored in the $\alpha 1$ compartment.
506 Compared to other DANs for appetitive memory, the DANs in the $\alpha 1$ only weakly respond
507 to sugar (Yamagata et al., 2015), and write a memory slowly even when optogenetically
508 activated (Aso and Rubin, 2016; Yamada et al., 2023). Once formed with repetitive
509 training, the memory in the $\alpha 1$ lasts over a day and is most resistant to extinction and
510 decay over time (Aso and Rubin, 2016; Huetteroth et al., 2015; Ichinose et al., 2015;
511 Yamada et al., 2023; Yamagata et al., 2015). These features collectively indicate that flies
512 undergo wind-guided olfactory navigation only when they expect a robust/reliable reward
513 (Figure 1E).

514 Second, the MB must operate with different downstream circuits in adults and
515 larva. Holometabolous insects undergo complete metamorphosis by which body structures
516 of larvae abruptly develop into adult's form through pupal stage. In *Drosophila*, behavioral
517 components of olfactory navigation and relevant neural circuits also undergo striking
518 changes through metamorphosis. *Drosophila* larvae hatch from eggs with already
519 developed circuits of olfaction and an MB that consists of ~70 mature KCs, 7 DANs and 24
520 MBONs (Eichler et al., 2017). The first instar larval MB circuit is numerically simpler than
521 that of the adult but can support associative learning (Pauls et al., 2010). Larval
522 *Drosophila* perform innate and memory-based olfactory navigation by modulating rate of
523 head casting and reorientation based on concentration gradient of odors measured over
524 time (Fishilevich et al., 2005; Saumweber et al., 2018). Although larvae can sense wind
525 and use it to avoid aversive odors (Jovanic et al., 2019), they do not use the wind direction
526 to localize the source of attractive odors as adults do. The adult airflow-sensing organ (i.e.,

527 aristae), relevant neural circuits such as the central complex, legs and wings all develop
528 during metamorphosis. Therefore, the metamorphosing MB circuit must adopt new
529 interacting partners to transform stored memories into adult-specific anemotaxis
530 behaviors.

531 The EM connectome of larval and adult MB circuits revealed many cell types with
532 similar morphology, which are in some cases labeled by the same genetic driver lines (Aso
533 et al., 2014a; Eichler et al., 2017; Li et al., 2020). To unambiguously match larval and adult
534 cell types, a recent study followed full developmental trajectories of larval MB cell types
535 into the adult MB by immobilizing expression patterns of genetic driver lines (Truman et
536 al., 2023). Intriguingly, a large fraction of MBONs and DANs survive through
537 metamorphosis and become a part of the adult MB circuit. For instance, among 17 types
538 of larval MBONs examined, 10 types developed into adult MBONs. These larval-origin
539 MBONs arborize their dendrites in the γ or β' lobes. Our experiments indicated that
540 appetitive memories in $\gamma 4$ and $\gamma 5\beta'2a$ compartments can bias the choice between
541 quadrants filled with CS+ and CS- odors but do not promote walking toward upwind
542 (Figure 1). This could be because the γ lobe stores both olfactory and visual memories
543 (Vogt et al., 2016, 2014); walking upwind does not help get closer to visual cues
544 associated with reward. On the other hand, α/β KCs, MBON- $\alpha 1$, MBON- $\alpha 3$, MBON- $\beta 1>\alpha$
545 are adult specific cell types. Notably, MBON- $\beta 1>\alpha$ innervates the α lobe and is directly
546 connected with MBON- $\alpha 1$ and MBON- $\alpha 3$, suggesting that UpWiNs may integrate
547 information from the $\beta 1$, $\alpha 1$ and $\alpha 3$. These anatomical observations suggest that the adult-
548 specific output pathways of MB may be dedicated to anemotaxis. In naturalistic olfactory
549 conditioning with sugar reward, flies form parallel appetitive memories in compartments of
550 both larval-origin and adult-specific MBONs. Future EM-connectome-guided studies will

551 elucidate how the adult MB integrates parallel memories to synthesize navigational
552 strategies by blending anemotactic and other behavioral components.

553

554 **Acknowledgments**

555 We thank Gerald M. Rubin, Glenn Turner, Ashok Litwin-Kumar, Daisuke Hattori, Gow
556 Turvo, Huai-ti Lin and members of the Y.A. and T.H. labs for valuable discussion and
557 comments on the manuscript. We thank Feng Li, Marisa Dreher, Christina Christoforou,
558 Kari Close and the members of Janelia FlyEM, Flylight, fly facility, Project Technical
559 Resource and scientific computing for technical support. D.Y. was supported by Toyobo
560 Biotechnology Foundation Postdoctoral Fellowship and Japan Society for the Promotion
561 of Science Overseas Research Fellowship. Y.A. was supported by HHMI. T.H. was
562 supported by NIH (R01DC018874), NSF (2034783), BSF (2019026) and UNC Junior
563 Faculty Development Award.

564 **Declaration of interests**

565 The authors declare no competing interests.

566 **CONTACT FOR REAGENT AND RESOURCE SHARING**

567 Further information and requests for resources and reagents should be directed to and will
568 be fulfilled by Yoshinori Aso (asoy@janelia.hhmi.org) or Toshihide Hige
569 (hige@email.unc.edu)

570 **Materials and Methods**

571

572 **Fly strains**

573 *Drosophila melanogaster* strains were reared at 22°C and 60% humidity on standard
574 cornmeal food in a 12:12 hour light:dark cycle. 4-10-day-old adult females were used 2-4
575 days after sorting them on a Peltier cold plate. For flies expressing CsChrimson (Klapoetke
576 et al., 2014) the food was supplemented with retinal (0.2 mM all-trans-retinal prior to
577 eclosion and then 0.4 mM). Driver and effector lines are listed in KEY RESOURCE TABLE
578 and genotypes used by each figure are listed below. The new collection of split-GAL4

579 drivers was designed based on confocal image databases (<http://flweb.janelia.org>)(Jenett
580 et al., 2012), and screening expression patterns of p65ADZp and ZpGAL4DBD
581 combinations as described previously (Aso et al., 2014a; Pfeiffer et al., 2010) and in the
582 accompanying article (Shuai et al., 2023). Confocal stacks of new split-GAL4 driver lines
583 used in this study are available at <http://www.janelia.org/split-gal4>.

584 **Olfactory conditioning**

585 Olfactory conditioning was performed as previously described (Aso and Rubin, 2016).
586 Groups of approximately 20 females of 4–10 d post-eclosion were trained and tested
587 using the modified four-field olfactory arena (Aso and Rubin, 2016; Pettersson, 1970)
588 equipped with a 627nm LED board (34.9 μ W/mm² at the position of the flies) and odor
589 mixers. The flow rate of input air from each of the four arms was maintained at
590 100 mL/min throughout the experiments by mass-flow controllers, and air was pulled
591 from the central hole at 400 mL/min. Odors were delivered to the arena by switching the
592 direction of airflow to the tubes containing diluted odors using solenoid valves. The odors
593 were diluted in paraffin oil: pentyl acetate (PA: 1:10000) and ethyl lactate (EL: 1:10000).
594 Sugar conditioning was performed by using tubes with sucrose absorbed Whatman 3
595 MM paper that was dried before use as previously described (Krashes and Waddell,
596 2008; Liu et al., 2012). For conditioning with optogenetic activation of DANs, 60 s of odor
597 was paired with 30 times 1 s of red LED light with 1-s gaps. LED pulses started 5 s after
598 the opening of odor valves. Before conditioning, flies were starved for 40-48 hour on 1%
599 agar. Videography was performed at 30 frames per second and analyzed using
600 Flytracker (<https://github.com/kristinbranson/FlyTracker>) or Fiji. For experiments using
601 one day memory retention, flies were kept in agar vials at 21°C after first-order
602 conditioning. For testing olfactory memories, the distribution of flies in the four quadrants
603 was measured for 60 s. The performance index (PI) is defined as a mean of [(number of
604 flies in the two diagonal quadrants filled with odor one) - (number of flies in other two
605 quadrants filled with odor two or air)]/(total number of flies) during the final 30 s of the
606 60-s test period. The average PI of reciprocal experiments is shown in figures to cancel
607 out potential position bias and innate odor preference.

608 **Airflow response**

609 For testing airflow directional response, each fly's distance from center (r_i) was
610 measured. The radius of the arena, r_{arena} , was 50 mm. Because of the circular shape of
611 the arena, the area of particular r bin is larger as r increases. For instance, the area of
612 40< r <50mm is 9 times larger than the area of 0< r <10 mm. When flies distribute
613 randomly in the arena, the mean r_i is $1/\sqrt{2}$. To normalize this area difference we used
614 the square of (r_i/r_{arena}) as an area-normalized distance from the center index. To
615 calculate upwind displacement, the mean of area-normalized distance from center at
616 each time point in each movie was subtracted by the area-normalized distance at the
617 onset of activating illumination or odor presentation. To compensate for the delay
618 between the switch of solenoid valves and delivery of the odor (~2 s) as well as the time
619 to fill the arena with odorized air (~3 s), the onset of odor was taken to be 3.5 seconds
620 after the switch of solenoid valves. For analysis of individual trajectories, only flies that
621 were more than 3 mm away from the edge of the arena were analyzed. Trajectories with
622 too abrupt changes of angle (more than 180 degree) or position (more than 5mm) in one
623 frame were considered as tracking errors and excluded from the analysis. The direction
624 toward the center of the arena, where suction tubing is connected, was designed as +/-

625 180 degrees relative to the upwind direction. For analyzing the influence of initial
626 orientation on directional turning and forward walking speed, subsets of trajectories were
627 analyzed by grouping them into +/- 30-degree bins of initial angle.

628

629 **Electrophysiology**

630 Electrophysiological experiments were performed as previously described (Yamada et al.,
631 2023). Briefly, flies were collected on the day of eclosion and kept in the dark on all-trans-
632 retinal food (0.5 mM) until experiments for 48-72 hr. The patch pipettes (6-7 MΩ) were
633 filled with the pipette solution containing (in mM): L-potassium aspartate, 140; HEPES, 10;
634 EGTA, 1.1; CaCl₂, 0.1; Mg-ATP, 4; Na-GTP, 0.5 with pH adjusted to 7.3 with KOH (265
635 mOsm). The preparation was continuously perfused with saline containing (in mM): NaCl,
636 103; KCl, 3; CaCl₂, 1.5; MgCl₂, 4; NaHCO₃, 26; N-tris(hydroxymethyl) methyl-2-
637 aminoethane-sulfonic acid, 5; NaH₂PO₄, 1; trehalose, 10; glucose, 10 (pH 7.3 when
638 bubbled with 95% O₂ and 5% CO₂, 275 mOsm). UpWiNs were visually identified by
639 fluorescence signals expressed by specific drivers. Whole-cell recordings were made
640 using the Axon MultiClamp 700B amplifier (Molecular Devices). Cells were held at around
641 -60 mV by injecting hyperpolarizing current, which was typically less than 10 pA. Signals
642 were low-pass filtered at 5 kHz and digitized at 10 kHz before being acquired and
643 analyzed by custom MATLAB scripts (MathWorks). Subthreshold odor responses were
644 quantified by averaging the mean depolarization above the baseline during 0 to 1.2 s after
645 odor onset. Saturated head-space vapors of odors were presented to flies after 1 % air
646 dilution using a custom odor delivery system. 625 nm LEDs were used to deliver
647 photostimulation at 17 mW/mm² through the objective lens.
648

649 **Calcium imaging**

650 All experiments were performed on female flies, 3-7 days after eclosion. Brains were
651 dissected in a saline bath (103 mM NaCl, 3 mM KCl, 2 mM CaCl₂, 4 mM MgCl₂, 26 mM
652 NaHCO₃, 1 mM NaH₂PO₄, 8 mM trehalose, 10 mM glucose, 5 mM TES, bubbled with
653 95% O₂ / 5% CO₂). After dissection, the brain was positioned anterior side up on a
654 coverslip in a Sylgard dish submerged in 3 ml saline at 20°C. The sample was imaged with
655 a resonant scanning 2-photon microscope with near-infrared excitation (920 nm, Spectra-
656 Physics, INSIGHT DS DUAL) and a 25X objective (Nikon MRD77225 25XW). The
657 microscope was controlled using ScanImage 2016 (Vidrio Technologies). Images were
658 acquired over a 231 μm × 231 μm x 42 μm volume with a step size at 2 μm. The field of
659 view included 512 × 512 pixel resolution taken at approximately 1.07 Hz frame rate. The
660 excitation power during imaging was 19 mW (Figure 4C) or 12 mW (Figure 4 – figure
661 supplement 1).

662 For photostimulation, the light-gated ion channel Chrimson88 (Klapoetke et al., 2014)
663 was activated with a 660-nm LED (M660L3 Thorlabs) coupled to a digital micromirror
664 device (Texas Instruments DLPC300 Light Crafter) and combined with the imaging path
665 using a FF757-DiO1 dichroic (Semrock). On the emission side, the primary dichroic was
666 DiO2-R635 (Semrock), the detection arm dichroic was 565DCXR (Chroma), and the
667 emission filters were FF03-525/50 and FF01-625/90 (Semrock). Photostimulation occurred
668 over a 1-s period at a 12 μW/mm² (Figure 4C) or 7.8 μW/mm² (Figure 4 – figure
669 supplement 1) intensity over 9 consecutive trials interspersed by a 30-s period. The light
670 intensity was measured using a Thorlabs S170C power sensor.

671 When quantifying the GCaMP fluorescence, ROIs corresponding to mushroom body
672 compartments were drawn using custom python scripts on images showing the maximum
673 intensity over time. Mean intensity changes within these ROIs were measured in the time

674 series images. Final intensity measurements subtracted a background ROI that was drawn
675 in a region with no fluorescence. Baseline fluorescence is the mean fluorescence over a 5-
676 s time period before stimulation started. The ΔF was then divided by baseline to normalize
677 the signal ($\Delta F/F$). The mean responses from the 9 trials were calculated for each animal (5-
678 11 samples per driver). Although RNAi should knockdown GCaMP6s expression in
679 UpWiNs expressing Chrimson88-tdTomato in Figure 4 – figure supplement 1, voxels
680 including neurons expressing red fluorescence (tdTomato) were excluded from the
681 analysis. This exclusion was performed by manually selecting a minimum threshold that
682 identified red fluorescent regions corresponding to tdTomato expressing neurons. Voxels in
683 the red channel above this threshold were excluded in the green channel measuring
684 GCaMP6s fluorescence.

685

686 **Analysis of connectivity and morphology**

687 The information was retrieved from neuPrint (neuprint.janelia.org) hosting the “hemibrain”
688 dataset (Scheffer et al., 2020), which is a publicly accessible web site
689 (<https://doi.org/10.25378/janelia.12818645.v1>). For cell types, we cited cell type
690 assignments reported in Scheffer et al., 2020. Only connections of the cells in the right
691 hemisphere were used due to incomplete connectivity in the left hemisphere (Zheng et al.,
692 2018). Connectivity data was then imported into Cytoscape (<https://cytoscape.org/>) for
693 generating circuit diagrams that were edited using Adobe Illustrator. The 3D renderings of
694 neurons presented were generated using the visualization tools of NeuTu (Zhao et al.,
695 2018) or VVD viewer (https://github.com/takashi310/VVD_Viewer;(Wan et al., 2012)).
696 Morphological similarity of individual neurons in SS33917 driver was performed by
697 NBLAST (Costa et al., 2016).

698

699 **Immunohistochemistry**

700 Brains and ventral nerve cord of 4-10 days old females were dissected, fixed and
701 immunolabeled as previously described using the antibodies listed in Key Resource
702 Table(Aso et al., 2014a; Nern et al., 2015).

703

704 **Statistics**

705 Statistical comparisons were performed on Graphpad Prism or MATLAB using the Kruskal
706 Wallis test followed by Dunn's post-test for multiple comparison, t-tests, or two-way ANOVA
707 followed by Tukey's post hoc multiple comparisons test as designated in figure legends.

708

709

710 **Detailed fly genotypes used by figures**

Figure	Genotype
Figure 1D-F	w/w, 20xUAS-CsChrimson-mVenus attP18;+;Gr64f-split-GAL4 (SS87269)
Figure 1H-L Figure 1-Figure supplement 1	w/w, 20xUAS-CsChrimson-mVenus attP18;+;MB043C-split-GAL4 w/w, 20xUAS-CsChrimson-mVenus attP18;+;MB213B-split-GAL4 w/w, 20xUAS-CsChrimson-mVenus attP18;+;MB312C-split-GAL4 w/w, 20xUAS-CsChrimson-mVenus attP18;MB109B/MB315C-split-GAL4

	<i>w/w, 20xUAS-CsChrimson-mVenus attP18;+/ Empty-split-GAL4</i>
Figure 2 Figure 2 -figure supplement 1 and 2	<i>w/w, 20xUAS-CsChrimson-mVenus attP18;Split-GAL4/+</i>
Figure 3A	<i>w/w, 20xUAS-CsChrimson-mVenus attP18;SS33917-Split-GAL4/+</i>
Figure 3 - figure supplement 2	<i>pBPhsFlp2::PEST in attP3;; pJFRC201-10XUAS-FRT>STOP>FRT-myR::smGFP-HA in VK0005, pJFRC240-10XUAS-FRT>STOP>FRT-myR::smGFP-V5-THS-10XUAS-FRT>STOP>FRT-myR::smGFP-FLAG in su(Hw)attP1/SS33917-split-GAL4</i>
Figure 4A	<i>LexAop2-Syn21-opGCaMP6s (JK16F), LexAop2-Syn21-opGCaMP6s (SuHwattP8), 10XUAS-Syn21-Chrimson88-tdT-3.1 (attP18)/+; R64A11-LexAp65 (JK73A)/MB082C</i>
Figure 4B	<i>LexAop2-Syn21-opGCaMP6s (JK16F), LexAop2-Syn21-opGCaMP6s (SuHwattP8), 10XUAS-Syn21-Chrimson88-tdT-3.1 (attP18)/+; R64A11-LexAp65 (JK73A)/MB310C</i>
Figure 4C	<i>LexAop2-Syn21-opGCaMP6s (JK16F), LexAop2-Syn21-opGCaMP6s (SuHwattP8), 10xUAS-Syn21-Chrimson88-tdT-3.1 (attP18); G0239-GAL4/G0239-GAL4; R64A11-LexAp65 (JK73A)/+</i> <i>LexAop2-Syn21-opGCaMP6s (JK16F), LexAop2-Syn21-opGCaMP6s (SuHwattP8), 10xUAS-Syn21-Chrimson88-tdT-3.1 (attP18); G0239-GAL4/G0239-GAL4; R64A11-LexAp65 (JK73A)/MB310C</i> <i>LexAop2-Syn21-opGCaMP6s (JK16F), LexAop2-Syn21-opGCaMP6s (SuHwattP8), 10xUAS-Syn21-Chrimson88-tdT-3.1 (attP18); G0239-GAL4/+; R64A11-LexAp65 (JK73A)/MB310C</i>
Figure 4 - figure supplement 1	<i>LexAop2-Syn21-opGCaMP6s in su(Hw)attP8, 10XUAS-Syn21-Chrimson88-tdT-3.1 in attP18; 10XUAS-LexAp65-DBD2-RNAi (VK2)/; 64A11-LexAp65</i>

	JK73A/ SS67249
Figure 5	<i>13XLexAop2-IVS-p10-ChrimsonR-mVenus (attP18); 58E02-LexAp65 (attP40)/ss67249-split1; pJFRC28-10XUAS-IVS-GFP-p10 (SuHwattP1) / ss67249-split2</i>
Figure 5 -figure supplement 1	<i>pBPhsFlp2::PEST in attP3;; pJFRC201-10XUAS-FRT>STOP>FRT-myr::smGFP-HA in VK0005, pJFRC240-10XUAS-FRT>STOP>FRT-myr::smGFP-V5-THS-10XUAS-FRT>STOP>FRT-myr::smGFP-FLAG in su(Hw)attP1/SS67249-split-GAL4</i>
Figure 5 -figure supplement 2	<i>13XLexAop2-IVS-p10-ChrimsonR-mVenus (attP18); 58E02-LexAp65 (attP40)/ss67249-split1; pJFRC28-10XUAS-IVS-GFP-p10 (SuHwattP1) / ss67249-split2</i>
Figure 6	<i>w/w, 20xUAS-CsChrimson-mVenus attP18;SS33917-Split-GAL4/+ w/w, 20xUAS-CsChrimson-mVenus attP18;SS33918-Split-GAL4/+ w/w, 20xUAS-CsChrimson-mVenus attP18;MB077B-Split-GAL4/+ w/w, 20xUAS-CsChrimson-mVenus attP18;Empty-Split-GAL4/+</i>
Figure 6 -figure supplement 1	<i>w/w, 20xUAS-CsChrimson-mVenus attP18;Split-GAL4/+</i>
Figure 7A-B	<i>w/+;SS33917-split-GAL4/+ w/+; SS33917-split-GAL4UAS-TNT (II) w/+; Empty-split-GAL4UAS-TNT (II)</i>
Figure 7C	<i>w/w;VT007746-p65ADZp in attP40/20xUAS-Shbire-p10 in VK00005 w/w;R64A11-ZpGAL4DBD in attP2/20xUAS-Shbire-p10 in VK00005 w/w;SS33917(VT007746-p65ADZp in attP40; R64A11-ZpGAL4DBD in attP2)/20xUAS-Shbire-p10 in VK00005 w/w;Empty-split-GAL4/20xUAS-Shbire-p10 in VK00005</i>
Figure 7D	<i>w/w, 20xUAS-CsChrimson-mVenus attP18;SS33917/+ w/w, 20xUAS-CsChrimson-mVenus</i>

	<i>attP18;Empty-split-GAL4</i> /+
Figure 7E	w/w, 20xUAS-CsChrimson-mVenus <i>attP18;SS33917</i> /+ w/w, 20xUAS-CsChrimson-mVenus <i>attP18;SS33918</i> /+ w/w, 20xUAS-CsChrimson-mVenus <i>attP18;SS49755</i> /+ w/w, 20xUAS-CsChrimson-mVenus <i>attP18;Empty-split-GAL4</i> /+
Figure 7 -figure supplement 1	w/w, 20xUAS-CsChrimson-mVenus <i>attP18;SS33917</i> /+ w/w, 20xUAS-CsChrimson-mVenus <i>attP18;SS33918</i> /+ w/w, 20xUAS-CsChrimson-mVenus <i>attP18;SS49755</i> /+ w/w, 20xUAS-CsChrimson-mVenus <i>attP18;Gr64f-GAL4;Gr64f-GAL4</i> /+ w/w, 20xUAS-CsChrimson-mVenus <i>attP18;Empty-split-GAL4</i> /+

711 **Data and Code Availability**

712 The confocal images of expression patterns are available online
 713 (<http://www.janelia.org/split-gal4>). The values used for figures are summarized in Source
 714 Data. The design files of the olfactory arena are available at flintbox
 715 (<https://hhmi.flintbox.com/technologies/c65b2ddd-3cc1-44d9-a95d-73e08723f724>).

716 **Supplemental information**

717

718

719 **Video 1. Activation phenotype of UpWiNs**

720 An example movie of UpWiN activation in SS33917>CsChrimson flies used in Figure 2.
 721 The red square at the bottom right corner indicates the 10-s period when the red LED was
 722 turned on. The small circles indicate the centroid of flies and triangles indicate the
 723 orientation of flies.

724

725

726 **Video 2. Activation phenotype of UpWiNs depends on the initial orientation**

727 Cropped movies of individual SS33917>CsChrimson flies centered and reoriented based
 728 on the position and the angle to upwind at the onset of the activating illumination (related to
 729 Figure 2 and Figure 6D-G). The red square at the bottom right corner of each panel
 730 indicates when the red LED was turned on. The small circles indicate the centroid of flies
 731 and triangles indicate the orientation of flies. The airflow direction was from the top to the
 732 bottom of each panel.

733

734 **Video 3. Convergent projection of MBON- α 1 and MBON- α 3 onto the dendritic area of
735 UpWiNs**

736 Overlay of MBON- α 1, MBON- α 3 and UpWiNs in a standard brain. UpWiNs were originally
737 identified by searching neurons that overlap with convergent axonal projection of these
738 MBONs using a database of confocal microscope images to generate split-GAL4 driver
739 lines.

740

741 **Video 4. Activation phenotype of UpWiNs without airflow**

742 An example movie of UpWiN activation in SS33917>CsChrimson flies without airflow
743 (related to Figure 6B).

744

745

746 **Video 5. Activation phenotype of UpWiNs depends on the intact aristae**

747 An example UpWiN activation phenotype in an SS33917>CsChrimson fly that lacked the
748 arista on the right side (related to Figure 6C).

749

750 **Video 6. Return phenotype induced by SMP357-362 activation**

751

752 An example movie of SMP357-362 activation in SS49755>CsChrimson flies. The red
753 square at the bottom right corner indicates the 10-s period when the red LED was turned
754 on. The small circles indicate the centroid of flies and triangles indicate the orientation of
755 flies. Trajectories of flies after turning off LED are shown as lines connecting centroids over
756 time.

757

758

759

760 **Supplementary File 1: KEY RESOURCES TABLE**

761

762

763

764

765 **References**

766 Álvarez-Salvado E, Licata AM, Connor EG, McHugh MK, King BMN, Stavropoulos N,
767 Victor JD, Crimaldi JP, Nagel KI. 2018. Elementary sensory-motor transformations
768 underlying olfactory navigation in walking fruit-flies. *eLife* 7:e37815.

769 Aso Y, Hattori D, Yu Y, Johnston RM, Iyer NA, Ngo T-TB, Dionne H, Abbott LF, Axel R,
770 Tanimoto H, Rubin GM. 2014a. The neuronal architecture of the mushroom body
771 provides a logic for associative learning. *eLife* 3:e04577.

772 Aso Y, Herb A, Ogueta M, Siwanowicz I, Templier T, Friedrich AB, Ito K, Scholz H,
773 Tanimoto H. 2012. Three dopamine pathways induce aversive odor memories with
774 different stability. *PLoS Genet* 8:e1002768.

775 Aso Y, Rubin GM. 2016. Dopaminergic neurons write and update memories with cell-
776 type-specific rules. *eLife* 5. doi:10.7554/eLife.16135

777 Aso Y, Sitaraman D, Ichinose T, Kaun KR, Vogt K, Belliard-Guérin G, Plaçais P-Y, Robie
778 AA, Yamagata N, Schnaitmann C, Rowell WJ, Johnston RM, Ngo T-TB, Chen N,
779 Korff W, Nitabach MN, Heberlein U, Preat T, Branson KM, Tanimoto H, Rubin GM.
780 2014b. Mushroom body output neurons encode valence and guide memory-based
781 action selection in *Drosophila*. *eLife* 3:e04580.

782 Baker TC. 1990. Upwind flight and casting flight : Complementary phasic and tonic
783 systems used for location of sex pheromone sources by male moth. *Proc 10th Int*

- 784 *Symp Olfaction and Taste, Oslo* **18-25**.
- 785 Berry JA, Phan A, Davis RL. 2018. Dopamine Neurons Mediate Learning and Forgetting
786 through Bidirectional Modulation of a Memory Trace. *Cell Rep* **25**:651–662.e5.
- 787 Besson M, Martin J-R. 2005. Centrophobism/thigmotaxis, a new role for the mushroom
788 bodies in *Drosophila*. *J Neurobiol* **62**:386–396.
- 789 Beyeler A, Namburi P, Glober GF, Simonnet C, Calhoon GG, Conyers GF, Luck R,
790 Wildes CP, Tye KM. 2016. Divergent Routing of Positive and Negative Information
791 from the Amygdala during Memory Retrieval. *Neuron* **90**:348–361.
- 792 Bogovic JA, Otsuna H, Heinrich L, Ito M, Jeter J, Meissner G, Nern A, Colonell J,
793 Malkesman O, Ito K, Saalfeld S. 2020. An unbiased template of the *Drosophila* brain
794 and ventral nerve cord. *PLoS One* **15**:e0236495.
- 795 Campbell RAA, Honegger KS, Qin H, Li W, Demir E, Turner GC. 2013. Imaging a
796 population code for odor identity in the *Drosophila* mushroom body. *J Neurosci*
797 **33**:10568–10581.
- 798 Cardé RT. 2021. Navigation Along Windborne Plumes of Pheromone and Resource-
799 Linked Odors. *Annu Rev Entomol* **66**:317–336.
- 800 Cohn R, Morantte I, Ruta V. 2015. Coordinated and Compartmentalized
801 Neuromodulation Shapes Sensory Processing in *Drosophila*. *Cell* **163**:1742–1755.
- 802 Costa M, Manton JD, Ostrovsky AD, Prohaska S, Jefferis GSXE. 2016. NBLAST: Rapid,
803 Sensitive Comparison of Neuronal Structure and Construction of Neuron Family
804 Databases. *Neuron* **91**:293–311.
- 805 Das G, Klappenbach M, Vrontou E, Perisse E, Clark CM, Burke CJ, Waddell S. 2014.
806 *Drosophila* learn opposing components of a compound food stimulus. *Curr Biol*
807 **24**:1723–1730.
- 808 Dolan M-J, Belliard-Guérin G, Bates AS, Frechter S, Lampin-Saint-Amaux A, Aso Y,
809 Roberts RV, Schlegel P, Wong A, Hammad A, Bock D, Rubin GM, Preat T, Plaçais
810 P-Y, Jefferis GSXE. 2018. Communication from Learned to Innate Olfactory
811 Processing Centers Is Required for Memory Retrieval in *Drosophila*. *Neuron*
812 **100**:651–668.e8.
- 813 Eckstein N, Bates AS, Du M, Hartenstein V, Jefferis GSX, Funke J. n.d.
814 Neurotransmitter Classification from Electron Microscopy Images at Synaptic Sites
815 in *Drosophila*. doi:10.1101/2020.06.12.148775
- 816 Eichler K, Li F, Litwin-Kumar A, Park Y, Andrade I, Schneider-Mizell CM, Saumweber T,
817 Huser A, Eschbach C, Gerber B, Fetter RD, Truman JW, Priebe CE, Abbott LF,
818 Thum AS, Zlatic M, Cardona A. 2017. The complete connectome of a learning and
819 memory centre in an insect brain. *Nature*. doi:10.1038/nature23455
- 820 Felsenberg J, Jacob PF, Walker T, Barnstedt O, Edmondson-Stait AJ, Pleijzier MW, Otto
821 N, Schlegel P, Sharifi N, Perisse E, Smith CS, Lauritzen JS, Costa M, Jefferis
822 GSXE, Bock DD, Waddell S. 2018. Integration of Parallel Opposing Memories
823 Underlies Memory Extinction. *Cell* **175**:709–722.e15.
- 824 Fishilevich E, Domingos AI, Asahina K, Naef F, Vosshall LB, Louis M. 2005. Chemotaxis
825 behavior mediated by single larval olfactory neurons in *Drosophila*. *Curr Biol*
826 **15**:2086–2096.
- 827 Gore F, Schwartz EC, Brangers BC, Aladi S, Stujenske JM, Likhtik E, Russo MJ, Gordon
828 JA, Salzman CD, Axel R. 2015. Neural Representations of Unconditioned Stimuli in
829 Basolateral Amygdala Mediate Innate and Learned Responses. *Cell* **162**:134–145.
- 830 Grewe BF, Gründemann J, Kitch LJ, Lecoq JA, Parker JG, Marshall JD, Larkin MC,
831 Jercog PE, Grenier F, Li JZ, Lüthi A, Schnitzer MJ. 2017. Neural ensemble
832 dynamics underlying a long-term associative memory. *Nature* **543**:670–675.
- 833 Handler A, Graham TGW, Cohn R, Morantte I, Siliciano AF, Zeng J, Li Y, Ruta V. 2019.
834 Distinct Dopamine Receptor Pathways Underlie the Temporal Sensitivity of

- 835 Associative Learning. *Cell* **178**:60–75.e19.
- 836 Heisenberg M. 2003. Mushroom body memoir: from maps to models. *Nat Rev Neurosci*
837 **4**:266–275.
- 838 Hige T. 2018. What can tiny mushrooms in fruit flies tell us about learning and memory?
839 *Neuroscience Research*. doi:10.1016/j.neures.2017.05.002
- 840 Hige T, Aso Y, Modi MN, Rubin GM, Turner GC. 2015a. Heterosynaptic Plasticity
841 Underlies Aversive Olfactory Learning in Drosophila. *Neuron* **88**:985–998.
- 842 Hige T, Aso Y, Rubin GM, Turner GC. 2015b. Plasticity-driven individualization of
843 olfactory coding in mushroom body output neurons. *Nature* **526**:258–262.
- 844 Huettneroth W, Perisse E, Lin S, Klappenbach M, Burke C, Waddell S. 2015. Sweet taste
845 and nutrient value subdivide rewarding dopaminergic neurons in Drosophila. *Curr
846 Biol* **25**:751–758.
- 847 Ichinose T, Aso Y, Yamagata N, Abe A, Rubin GM, Tanimoto H. 2015. Reward signal in
848 a recurrent circuit drives appetitive long-term memory formation. *Elife* **4**:e10719.
- 849 Ichinose T, Kanno M, Wu H, Yamagata N, Sun H, Abe A, Tanimoto H. 2021. Mushroom
850 body output differentiates memory processes and distinct memory-guided
851 behaviors. *Curr Biol* **31**:1294–1302.e4.
- 852 Jacob PF, Waddell S. 2022a. Spaced Training Forms Complementary Long-Term
853 Memories of Opposite Valence in Drosophila. *Neuron* **110**:2703.
- 854 Jacob PF, Waddell S. 2022b. Spaced Training Forms Complementary Long-Term
855 Memories of Opposite Valence in Drosophila. *Neuron* **110**:2703.
- 856 Jenett A, Rubin GM, Ngo T-TB, Shepherd D, Murphy C, Dionne H, Pfeiffer BD,
857 Cavallaro A, Hall D, Jeter J, Iyer N, Fetter D, Hausenfluck JH, Peng H, Trautman
858 ET, Svirskas RR, Myers EW, Iwinski ZR, Aso Y, DePasquale GM, Enos A, Hulamm
859 P, Lam SCB, Li H-H, Laverty TR, Long F, Qu L, Murphy SD, Rokicki K, Safford T,
860 Shaw K, Simpson JH, Sowell A, Tae S, Yu Y, Zugates CT. 2012. A GAL4-driver line
861 resource for Drosophila neurobiology. *Cell Rep* **2**:991–1001.
- 862 Jovanic T, Winding M, Cardona A, Truman JW, Gershow M, Zlatic M. 2019. Neural
863 Substrates of Drosophila Larval Anemotaxis. *Curr Biol* **29**:554–566.e4.
- 864 Kamikouchi A, Shimada T, Ito K. 2006. Comprehensive classification of the auditory
865 sensory projections in the brain of the fruit fly Drosophila melanogaster. *J Comp
866 Neurol* **499**:317–356.
- 867 Kanzaki R, Ikeda A. 1994. Morphology and Physiology of Pheromone-Triggered Flip-
868 Flopping Descending Interneurons of the Male Silkworm Moth, Bombyx mori.
869 *Olfaction and Taste XI*. doi:10.1007/978-4-431-68355-1_348
- 870 Kaun KR, Azanchi R, Maung Z, Hirsh J, Heberlein U. 2011. A Drosophila model for
871 alcohol reward. *Nature Neuroscience*. doi:10.1038/nn.2805
- 872 Kirkhart C, Scott K. 2015. Gustatory learning and processing in the Drosophila
873 mushroom bodies. *J Neurosci* **35**:5950–5958.
- 874 Kitamoto T. 2001. Conditional modification of behavior in Drosophila by targeted
875 expression of a temperature-sensitive shibire allele in defined neurons. *J Neurobiol*
876 **47**:81–92.
- 877 Klapoetke NC, Murata Y, Kim SS, Pulver SR, Birdsey-Benson A, Cho YK, Morimoto TK,
878 Chuong AS, Carpenter EJ, Tian Z, Wang J, Xie Y, Yan Z, Zhang Y, Chow BY,
879 Surek B, Melkonian M, Jayaraman V, Constantine-Paton M, Wong GK-S, Boyden
880 ES. 2014. Independent optical excitation of distinct neural populations. *Nat Methods*
881 **11**:338–346.
- 882 Krashes MJ, Waddell S. 2008. Rapid consolidation to a radish and protein synthesis-
883 dependent long-term memory after single-session appetitive olfactory conditioning
884 in Drosophila. *J Neurosci* **28**:3103–3113.
- 885 Li F, Lindsey JW, Marin EC, Otto N, Dreher M, Dempsey G, Stark I, Bates AS, Pleijzier

- 886 MW, Schlegel P, Nern A, Takemura S-Y, Eckstein N, Yang T, Francis A, Braun A,
887 Parekh R, Costa M, Scheffer LK, Aso Y, Jefferis GS, Abbott LF, Litwin-Kumar A,
888 Waddell S, Rubin GM. 2020. The connectome of the adult Drosophila mushroom
889 body provides insights into function. *Elife* **9**. doi:10.7554/eLife.62576
- 890 Lin S, Owald D, Chandra V, Talbot C, Huetteroth W, Waddell S. 2014. Neural correlates
891 of water reward in thirsty Drosophila. *Nat Neurosci* **17**:1536–1542.
- 892 Liu C, Plaçais P-Y, Yamagata N, Pfeiffer BD, Aso Y, Friedrich AB, Siwanowicz I, Rubin
893 GM, Prent T, Tanimoto H. 2012. A subset of dopamine neurons signals reward for
894 odour memory in Drosophila. *Nature* **488**:512–516.
- 895 Matheson AMM, Lanz AJ, Medina AM, Licata AM, Currier TA, Syed MH, Nagel KI. 2022.
896 A neural circuit for wind-guided olfactory navigation. *Nat Commun* **13**:4613.
- 897 McCurdy LY, Sareen P, Davoudian PA, Nitabach MN. 2021. Dopaminergic mechanism
898 underlying reward-encoding of punishment omission during reversal learning in
899 Drosophila. *Nat Commun* **12**:1115.
- 900 Modi MN, Shuai Y, Turner GC. 2020. The Mushroom Body: From Architecture to
901 Algorithm in a Learning Circuit. *Annu Rev Neurosci* **43**:465–484.
- 902 Namburi P, Beyeler A, Yorozu S, Calhoon GG, Halbert SA, Wichmann R, Holden SS,
903 Mertens KL, Anahtar M, Felix-Ortiz AC, Wickersham IR, Gray JM, Tye KM. 2015. A
904 circuit mechanism for differentiating positive and negative associations. *Nature*
905 **520**:675–678.
- 906 Nern A, Pfeiffer BD, Rubin GM. 2015. Optimized tools for multicolor stochastic labeling
907 reveal diverse stereotyped cell arrangements in the fly visual system. *Proc Natl
908 Acad Sci U S A* **112**:E2967–76.
- 909 Nieh EH, Vander Weele CM, Matthews GA, Presbrey KN, Wichmann R, Leppla CA,
910 Izadmehr EM, Tye KM. 2016. Inhibitory Input from the Lateral Hypothalamus to the
911 Ventral Tegmental Area Disinhibits Dopamine Neurons and Promotes Behavioral
912 Activation. *Neuron* **90**:1286–1298.
- 913 Okubo TS, Patella P, D'Alessandro I, Wilson RI. 2020. A Neural Network for Wind-
914 Guided Compass Navigation. *Neuron* **107**:924–940.e18.
- 915 O'Neill P-K, Gore F, Salzman CD. 2018. Basolateral amygdala circuitry in positive and
916 negative valence. *Curr Opin Neurobiol* **49**:175–183.
- 917 Otsuna H, Ito M, Kawase T. n.d. Color depth MIP mask search: a new tool to expedite
918 Split-GAL4 creation. doi:10.1101/318006
- 919 Owald D, Felsenberg J, Talbot CB, Das G, Perisse E, Huetteroth W, Waddell S. 2015.
920 Activity of defined mushroom body output neurons underlies learned olfactory
921 behavior in Drosophila. *Neuron* **86**:417–427.
- 922 Owald D, Waddell S. 2015. Olfactory learning skews mushroom body output pathways
923 to steer behavioral choice in Drosophila. *Curr Opin Neurobiol* **35**:178–184.
- 924 Pai T-P, Chen C-C, Lin H-H, Chin A-L, Lai JS-Y, Lee P-T, Tully T, Chiang A-S. 2013.
925 Drosophila ORB protein in two mushroom body output neurons is necessary for
926 long-term memory formation. *Proc Natl Acad Sci U S A* **110**:7898–7903.
- 927 Pascual A, Préat T. 2001. Localization of long-term memory within the Drosophila
928 mushroom body. *Science* **294**:1115–1117.
- 929 Pauls D, Selcho M, Gendre N, Stocker RF, Thum AS. 2010. Drosophila larvae establish
930 appetitive olfactory memories via mushroom body neurons of embryonic origin. *J
931 Neurosci* **30**:10655–10666.
- 932 Pettersson J. 1970. An Aphid Sex Attractant. *Insect Systematics & Evolution*.
933 doi:10.1163/187631270x00357
- 934 Pfeiffer BD, Ngo T-TB, Hibbard KL, Murphy C, Jenett A, Truman JW, Rubin GM. 2010.
935 Refinement of tools for targeted gene expression in Drosophila. *Genetics* **186**:735–
936 755.

- 937 Plaçais P-Y, Trannoy S, Friedrich AB, Tanimoto H, Preat T. 2013. Two pairs of
 938 mushroom body efferent neurons are required for appetitive long-term memory
 939 retrieval in Drosophila. *Cell Rep* **5**:769–780.
 940 Saumweber T, Rohwedder A, Schleyer M, Eichler K, Chen Y-C, Aso Y, Cardona A,
 941 Eschbach C, Kobler O, Voigt A, Durairaja A, Mancini N, Zlatic M, Truman JW, Thum
 942 AS, Gerber B. 2018. Functional architecture of reward learning in mushroom body
 943 extrinsic neurons of larval Drosophila. *Nat Commun* **9**:1104.
 944 Scaplen KM, Talay M, Fisher JD, Cohn R, Sorkaç A, Aso Y, Barnea G, Kaun KR. 2021.
 945 Transsynaptic mapping of mushroom body output neurons. *Elife* **10**.
 946 doi:10.7554/eLife.63379
 947 Scheffer LK, Xu CS, Januszewski M, Lu Z, Takemura S-Y, Hayworth KJ, Huang GB,
 948 Shinomiya K, Maitlin-Shepard J, Berg S, Clements J, Hubbard PM, Katz WT,
 949 Umayam L, Zhao T, Ackerman D, Blakely T, Bogovic J, Dolafi T, Kainmueller D,
 950 Kawase T, Khairy KA, Leavitt L, Li PH, Lindsey L, Neubarth N, Olbris DJ, Otsuna H,
 951 Trautman ET, Ito M, Bates AS, Goldammer J, Wolff T, Svirskas R, Schlegel P,
 952 Neace E, Knecht CJ, Alvarado CX, Bailey DA, Ballinger S, Borycz JA, Canino BS,
 953 Cheatham N, Cook M, Dreher M, Duclos O, Eubanks B, Fairbanks K, Finley S,
 954 Forknall N, Francis A, Hopkins GP, Joyce EM, Kim S, Kirk NA, Kovalyak J, Lauchie
 955 SA, Lohff A, Maldonado C, Manley EA, McLin S, Mooney C, Ndama M, Ogundeyi
 956 O, Okeoma N, Ordish C, Padilla N, Patrick CM, Paterson T, Phillips EE, Phillips EM,
 957 Rampally N, Ribeiro C, Robertson MK, Rymer JT, Ryan SM, Sammons M, Scott
 958 AK, Scott AL, Shinomiya A, Smith C, Smith K, Smith NL, Sobeski MA, Suleiman A,
 959 Swift J, Takemura S, Talebi I, Tarnogorska D, Tenshaw E, Tokhi T, Walsh JJ, Yang
 960 T, Horne JA, Li F, Parekh R, Rivlin PK, Jayaraman V, Costa M, Jefferis GS, Ito K,
 961 Saalfeld S, George R, Meinertzhagen IA, Rubin GM, Hess HF, Jain V, Plaza SM.
 962 2020. A connectome and analysis of the adult central brain. *Elife* **9**.
 963 doi:10.7554/eLife.57443
 964 Schnitzer M, Huang C, Luo J, Woo SJ, Roitman L, Li J, Pieribone V, Kannan M, Vasan
 965 G. n.d. Dopamine signals integrate innate and learnt valences to regulate memory
 966 dynamics. doi:10.21203/rs.3.rs-1915648/v1
 967 Séjourné J, Plaçais P-Y, Aso Y, Siwanowicz I, Trannoy S, Thoma V, Tedjakumala SR,
 968 Rubin GM, Tchénio P, Ito K, Isabel G, Tanimoto H, Preat T. 2011. Mushroom body
 969 efferent neurons responsible for aversive olfactory memory retrieval in Drosophila.
 970 *Nat Neurosci* **14**:903–910.
 971 Shuai Y, Sammons M, Sterne GR, Hibbard K, Yang H, Yang C-P, Managan C,
 972 Siwanowicz I, Lee T, Rubin GM, Turner GC, Aso Y. 2023. Driver lines for studying
 973 associative learning in Drosophila. *bioRxiv*. doi:10.1101/2023.09.15.557808
 974 Siju KP, Štih V, Aimon S, Gjorgjieva J, Portugues R, Grunwald Kadow IC. 2020. Valence
 975 and State-Dependent Population Coding in Dopaminergic Neurons in the Fly
 976 Mushroom Body. *Curr Biol* **30**:2104–2115.e4.
 977 Steck K, Veit D, Grandy R, Badia SBI, Badia SBI, Mathews Z, Verschure P, Hansson
 978 BS, Knaden M. 2012. A high-throughput behavioral paradigm for Drosophila
 979 olfaction - The Flywalk. *Sci Rep* **2**:361.
 980 Sun F, Zhou J, Dai B, Qian T, Zeng J, Li X, Zhuo Y, Zhang Y, Wang Y, Qian C, Tan K,
 981 Feng J, Dong H, Lin D, Cui G, Li Y. 2020. Next-generation GRAB sensors for
 982 monitoring dopaminergic activity in vivo. *Nat Methods* **17**:1156–1166.
 983 Suver MP, Matheson AMM, Sarkar S, Damiata M, Schoppik D, Nagel KI. 2019.
 984 Encoding of Wind Direction by Central Neurons in Drosophila. *Neuron* **102**:828–
 985 842.e7.
 986 Takemura S, Aso Y, Hige T, Wong A, Lu Z, Xu CS. 2017. A connectome of a learning
 987 and memory center in the adult Drosophila brain. *Elife*.

- 988 Tanaka NK, Tanimoto H, Ito K. 2008. Neuronal assemblies of the Drosophila mushroom
989 body. *J Comp Neurol* **508**:711–755.
- 990 Truman JW, Price J, Miyares RL, Lee T. 2023. Metamorphosis of memory circuits in
991 reveals a strategy for evolving a larval brain. *eLife* **12**. doi:10.7554/eLife.80594
- 992 Tully T, Quinn WG. 1985. Classical conditioning and retention in normal and mutant
993 *Drosophila melanogaster*. *J Comp Physiol A* **157**:263–277.
- 994 Tye KM. 2018. Neural Circuit Motifs in Valence Processing. *Neuron* **100**:436–452.
- 995 van Breugel F, Dickinson MH. 2014. Plume-tracking behavior of flying *Drosophila*
996 emerges from a set of distinct sensory-motor reflexes. *Curr Biol* **24**:274–286.
- 997 Vergassola M, Villermaux E, Shraiman BI. 2007. “Infotaxis” as a strategy for searching
998 without gradients. *Nature*. doi:10.1038/nature05464
- 999 Vet LEM, Van Lenteren JC, Heymans M, Meelis E. 1983. An airflow olfactometer for
1000 measuring olfactory responses of hymenopterous parasitoids and other small
1001 insects. *Physiological Entomology*. doi:10.1111/j.1365-3032.1983.tb00338.x
- 1002 Vogt K, Aso Y, Hige T, Knapek S, Ichinose T, Friedrich AB, Turner GC, Rubin GM,
1003 Tanimoto H. 2016. Direct neural pathways convey distinct visual information to
1004 *Drosophila* mushroom bodies. *eLife* **5**. doi:10.7554/eLife.14009
- 1005 Vogt K, Schnaitmann C, Dylla KV, Knapek S, Aso Y, Rubin GM, Tanimoto H. 2014.
1006 Shared mushroom body circuits underlie visual and olfactory memories in
1007 *Drosophila*. *eLife* **3**:e02395.
- 1008 Vrontou E, Groschner LN, Szydlowski S, Brain R, Krebbers A, Miesenböck G. 2021.
1009 Response competition between neurons and antineurons in the mushroom body.
1010 *Curr Biol* **31**:4911–4922.e4.
- 1011 Wan Y, Otsuna H, Chien C-B, Hansen C. 2012. FluoRender: An Application of 2D Image
1012 Space Methods for 3D and 4D Confocal Microscopy Data Visualization in
1013 Neurobiology Research. *IEEE Pac Vis Symp* 201–208.
- 1014 Yamada D, Bushey D, Li F, Hibbard KL, Sammons M, Funke J, Litwin-Kumar A, Hige T,
1015 Aso Y. 2023. Hierarchical architecture of dopaminergic circuits enables second-
1016 order conditioning in. *eLife* **12**. doi:10.7554/eLife.79042
- 1017 Yamagata N, Ichinose T, Aso Y, Plaçais P-Y, Friedrich AB, Sima RJ, Preat T, Rubin GM,
1018 Tanimoto H. 2015. Distinct dopamine neurons mediate reward signals for short- and
1019 long-term memories. *Proc Natl Acad Sci U S A* **112**:578–583.
- 1020 Yorozu S, Wong A, Fischer BJ, Dankert H, Kernan MJ, Kamikouchi A, Ito K, Anderson
1021 DJ. 2009. Distinct sensory representations of wind and near-field sound in the
1022 *Drosophila* brain. *Nature* **458**:201–205.
- 1023 Zars T, Fischer M, Schulz R, Heisenberg M. 2000. Localization of a short-term memory
1024 in *Drosophila*. *Science* **288**:672–675.
- 1025 Zhang X, Li B. 2018. Population coding of valence in the basolateral amygdala. *Nat
1026 Commun* **9**:1–14.
- 1027 Zhao T, Olbris DJ, Yu Y, Plaza SM. 2018. NeuTu: Software for Collaborative, Large-
1028 Scale, Segmentation-Based Connectome Reconstruction. *Front Neural Circuits*
1029 **12**:101.
- 1030 Zheng Z, Lauritzen JS, Perlman E, Robinson CG, Nichols M, Milkie D, Torrens O, Price
1031 J, Fisher CB, Sharifi N, Calle-Schuler SA, Kmecova L, Ali IJ, Karsh B, Trautman ET,
1032 Bogovic JA, Hanslovsky P, Jefferis GSXE, Kazhdan M, Khairy K, Saalfeld S, Fetter
1033 RD, Bock DD. 2018. A Complete Electron Microscopy Volume of the Brain of Adult
1034 *Drosophila melanogaster*. *Cell* **174**:730–743.e22.
- 1035 Zolin A, Cohn R, Pang R, Siliciano AF, Fairhall AL, Ruta V. 2021. Context-dependent
1036 representations of movement in *Drosophila* dopaminergic reinforcement pathways.
1037 *Nat Neurosci* **24**:1555–1566.

1038

1039

1040 **Figure Legends**

1041 **Figure 1. Memories in specific set of MB-compartments drive upwind locomotion**

1042 (A) A conceptual diagram of the mushroom body circuit. The colored rectangles
1043 represent individual MB compartments.

1044 (B) A diagram of a four-armed olfactory arena. In each experiment, approximately 20
1045 female flies were introduced into the circular arena.

1046 (C) Protocols for optogenetic training and tests used. One of two odors (PA and EL) was
1047 presented for 20 s, and three 1-s pulses of 627nm light were started at 14 s. Another
1048 odor was presented alone, and then preference between two odors was measured. The
1049 cycles of training and tests were repeated nine times. In the unpaired protocol, LED was
1050 started 90 s before the onset of “CS+” odor.

1051 (D) Preference to the CS+ odor in binary choice.

1052 (E) Displacement of flies’ position relative to the center of the arena during the initial 14 s
1053 of 20-s odor period as wind-directional response.

1054 (F) Learning rate defined as response after single training divided by peak response
1055 after 9x training.

1056 (G) Protocols for optogenetic training and the two different memory tests used in this
1057 work.

1058 (H) Appetitive memories assessed by binary choice between CS+ and CS- odors
1059 immediately after training with optogenetic activation of DANs that express CsChrimson
1060 with drivers indicated in I. empty is a split-GAL4 driver without promoters for AD and
1061 DBD domains. Thick and thin horizontal lines represent means and SEMs. Dunn’s
1062 multiple comparison tests compared to empty-split-GAL4 control, following Kruskal-
1063 Wallis test; n = 12-22.

1064 (I) Time course of the area-normalized mean of fly’s position relative to the center of the
1065 arena as compared with its mean position at odor onset and the cosine of the angle
1066 between the fly’s orientation and the upwind direction (See Methods). Flies of each
1067 genotype were trained with three protocols: 1) Petyl Acetate (PA) was paired with the
1068 LED illumination and Ethyl Lactate (EL) was unpaired. 2) EL was paired with LED and
1069 PA was unpaired. 3) Neither odor was paired (No LED). Lines and filled areas around
1070 lines are mean and SEM. n = 24-60.

1071 (J) The delta of distance from the center at the end of the 10-s odor period. Each dot
1072 represents data from individual trials. Black lines are mean and SEM. *, p<0.05; ***,
1073 p<0.001; Dunn’s multiple comparison tests compared to empty-split-GAL4 control,
1074 following Kruskal-Wallis test; n = 24-60. The upwind displacements of MB213B and
1075 MB043C in response to CS+ odor were also significantly higher than the control when
1076 trial averages of 6 movies were compared.

1077 (K) Cumulative angle of turning and forward walking speed during the first 10 frames
1078 (333 ms; a time window we used for optogenetic experiments in Figure 6) following odor
1079 onset are plotted against initial angle to upwind, smoothed with +/- 30-degree bin. The
1080 number of trajectories analyzed for (CS+, CS-, No LED) conditions for
1081 MB109B+MB315C, MB312C, MB213B and MB043C were (531, 562, 167), (710, 758,
1082 814), (920, 1039, 919) and (449, 768, 531), respectively. Only flies that were 3 mm or
1083 more from the edge of the arena were analyzed.

1084 (L) The violin-plots of the cumulative angle of turn to the upwind orientation during the

1085 first 10 frames (333 ms) of odor onset. Only flies that oriented -90 to -150 or +90 to 150
1086 degrees to the upwind direction at odor onset were analyzed. n = 122, 137, 233, 239, 99
1087 for empty-split-GAL4, MB109B+MB315C, MB312C, MB213B and MB043C, respectively.
1088 *, p<0.05; ***, p<0.001; Dunn's multiple comparison tests compared to empty-split-GAL4
1089 control, following Kruskal-Wallis test.

1090

1091 **Figure 1-figure supplement 1. Memory-based modulation of walking speed and**
1092 **angular speed depends on the fly's initial angle to the upwind direction**

1093 (A-E) The cosine of the angle to upwind direction, angular speed and forward walking
1094 speed are separately plotted for flies oriented downwind or upwind at odor onset (Time =
1095 0 s). Only flies that were at least 3 mm away from the edge of the arena were analyzed.
1096 The source data are identical to Figure 1E-H.

1097

1098 **Figure 2. Identification of UpWiNs by activation screening**

1099 (A) Mean displacement of fly's position relative to the center of the arena during
1100 activation of various cell types defined by the indicated driver lines. Red asterisks
1101 indicate the results of Dunn's multiple comparison tests compared to empty-split-GAL4
1102 control, following Kruskal-Wallis test;*, p<0.05; **, p<0.01; ***, p<0.001, n = 18-132;
1103 Black asterisks indicate p<0.05 without correction for multiple comparisons. The median,
1104 first and third quartiles, 10 and 90 percentiles are displayed with outlier data points. Each
1105 of 6 movies from a group of flies was considered as a single data point. The conclusions
1106 about the UpWiNs lines (i.e. SS33917 and SS33918) did not change when trial averages
1107 of 6 movies were used for statistical tests. See Figure 2-figure supplement 2 and
1108 <http://www.janelia.org/split-gal4> for expression patterns of CsChrimson in these driver
1109 lines.

1110 (B) Z-scores for five parameters for 2-s time bins (T1 to T2) before, during (bold
1111 numbers) and after the 10-s activation period. Z-scores for driver line were calculated by
1112 (value – mean)/(standard deviation). For calculating the probability of return, 15-s-long
1113 trajectories of each fly following each time point (t1) were analyzed. A fly was considered
1114 to revisit the original location at time0 if it moved away more than 10 mm and came back
1115 to within 3 mm distance from that location at time0 within 15 s. "time0" ranges 0 to 45-s,
1116 because the movies were 60s long. High Z-score at 8-10-s time bin indicate that flies
1117 tended to move back to their location at 8-10 s by 23-25 s (i.e. mostly dark period after
1118 LED was turned off).

1119 **Figure 2-figure supplement 1. Activation phenotypes of "hit" lines**

1120 Time courses of five behavioral parameters are shown for driver lines with significant
1121 upwind locomotion (i.e. delta distance from center) phenotypes in Figure 2. Lines and
1122 shaded areas around lines are mean and SEM for trial averages; split-
1123 GAL4>CsChrimson-mVenus are shown in blue and empty-split-Gal4>CsChrimson-
1124 mVenus in gray.

1125 **Figure 2-figure supplement 2. Expression patterns of "hit" lines**

1126 Projection of confocal microscopy stacks for expression patterns of CsChrimson-
1127 mVenus driven by designated split-GAL4 driver lines in brains and ventral nerve cords.
1128 Confocal stacks are available at <https://splitgal4.janelia.org>

1129 **Figure 2-figure supplement 3. LM-EM matching of cell types in SS49899**

1130 (A) The fan-shaped body neurons in SS49899 driver that were visualized with myr-
1131 smGFP-HA (green) and synaptotagmin-smGFP-V5 (magenta). The outlines of the
1132 standard brain and the mushroom body are shown in gray. Other driver lines with similar
1133 expression patterns are listed. Confocal stacks are available at
1134 <https://splitgal4.janelia.org>

1135 (B) The corresponding EM reconstructed neurons, which were matched by comparing
1136 projection patterns in the standard brain and referring MCFO images of split-GAL4.

1137 (A') and (B') are projections from dorsal side of the brains.

1138 **Figure 2-figure supplement 4. LM-EM matching of cell types in SS49755**

1139 (A) The SMP neurons in SS49755 driver that were visualized with myr-smGFP-HA
1140 (green) and synaptotagmin-smGFP-V5 (magenta). The outlines of the standard brain
1141 and the mushroom body are shown in gray. Other driver lines with similar expression
1142 patterns are listed.

1143 (B) The corresponding EM reconstructed neurons, which were matched by comparing
1144 projection patterns in the standard brain and referring MCFO images of split-GAL4.
1145 Confocal stacks are available at <https://splitgal4.janelia.org>

1146 (A') and (B') are projections from dorsal side of the brains.

1147

1148 **Figure 3. Connectivity of UpWiNs**

1149 (A) The expression pattern of CsChrimson-mVenus driven by split-GAL4 line SS33917.
1150 The insert image shows signals of membrane reporter myr-smHA and presynaptic
1151 reporter Syt-smV5 driven by the same driver.

1152 (B) Eleven EM-reconstructed neurons that correspond to UpWiNs defined by the
1153 SS33917 driver were identified by analyzing the morphology of individual neurons
1154 (Figure 3-figure supplement 1 and 2) and are displayed with outline of the MB and the
1155 standard brain. Individual neurons are color-coded to indicate the cell type to which they
1156 were assigned.

1157 (C) Connectivity of UpWiNs with major upstream and downstream neurons that have at
1158 least 20 connections with one of the 11 UpWiNs. The hemibrain body IDs of each
1159 neuron is shown as well as their assignment to specific cell types. Numbers indicate the
1160 number of synapses from the upstream neurons to UpWin neurons (left) or from the
1161 UpWiNs to the downstream neurons (right).

1162 (D) Interneurons downstream to MBON- α 1 and MBON- α 3. Colors of dots indicate
1163 neurotransmitter prediction (Eckstein et al., n.d.). See Figure 3-figure supplement 3 for
1164 more detail.

1165 (E) Predicted postsynaptic sites in SMP353 and SMP354 (gray), which are juxtaposed to
1166 presynaptic sites from MBON- α 1 (green) and MBON- α 3 (orange).

1167 (F) Interconnectivity between UpWiNs. The numbers indicate the summed number of
1168 connections. The numbers in parentheses indicate the number of neurons per cell type.

1169

1170 **Figure 3-figure supplement 1. Candidate UpWiNs in hemibrain EM images**

1171 (A) Frontal and dorsal projection of 11 EM-reconstructed neurons that were matched
1172 with confocal images of UpWiNs within the standard brain (Bogovic et al., 2020) (see
1173 Figure 3-figure supplement 2). Pseudo colors were assigned to each of five cell types.
1174 The arrowhead and arrow indicate common axonal tract and terminal area in the SMP.
1175 IDs of each neuron are displayed. The somas of these neurons are clustered near the tip
1176 of the vertical lobe of the MB, and they share the tracts for the primary neurite and
1177 axons, whereas the branching patterns of their dendrites exhibit cell-type-specific
1178 characteristics, which were used for cell type matching.
1179 (B-L) Projections of individual neurons. The arrows indicate dendritic branches that are
1180 characteristic to each cell type.

1181

1182

1183 **Figure 3-figure supplement 2. Single cell images of neurons in SS33917**

1184 (A-Y) Frontal projections of segmented multi-color flip-out images of SS33917 (colored)
1185 with corresponding EM neuron (gray). The arrows indicate dendritic branches that are
1186 characteristic to each cell type.

1187

1188 **Figure 3-figure supplement 3. NBLAST clustering of single cell images of neurons
1189 in SS33917**

1190 Multi-color flip-out (MCFO) single cell images of SS33917 driver were clustered into 6
1191 groups, which were nearly identical to the manual annotation.

1192

1193 **Figure 3-figure supplement 4. Downstream neurons of MBON- α 1 and MBON- α 3**

1194 Connectivity from MBON- α 1 and MBON- α 3 to downstream neurons that receive at least
1195 10 connections.

1196

1197

1198 **Figure 4. UpWiNs integrate excitatory and inhibitory synaptic inputs from MBONs.**

1199 (A) Functional connectivity between MBON- α 3 and UpWiNs. Chrimson88-tdTomato was
1200 expressed in MBON- α 3 by MB082C split-GAL4, and the photostimulation responses
1201 were measured by whole-cell current-clamp recording in randomly selected UpWiNs
1202 labeled by R64A11-LexA. 3 out of 11 neurons (7 flies) showed excitatory response. Mean
1203 voltage traces from individual connected (orange) and unconnected UpWiNs (gray) are
1204 overlaid. The connection was strong enough to elicit spikes (black; single-trial response
1205 in one of the connected UpWiNs). Magenta vertical line indicates photostimulation (10
1206 ms).

1207 (B) Functional connectivity between MBON- α 1 and UpWiNs. Chrimson88-tdTomato
1208 expression in MBON- α 1 was driven by MB310C split-GAL4. 4 out of 17 neurons (12
1209 flies) showed inhibitory response. Mean voltage traces from individual connected (green)
1210 and unconnected UpWiNs (gray) are overlaid.

1211 (C) Integration of synaptic inputs from MBON- α 3 and MBON- α 1. Population responses
1212 of UpWiNs were measured by two-photon calcium imaging at the junction between

1213 dendrites and axonal tracts (mean $\Delta F/F \pm SEM$) while photostimulating MBON- $\alpha 3$
1214 (orange; n = 5), MBON- $\alpha 1$ (green; n = 11) or both (black; n = 7). Expression of
1215 GCaMP6s was driven by R64A11-LexA, and Chrimson88-tdTomato by G0239-GAL4
1216 (MBON- $\alpha 3$) and/or MB310C (MBON- $\alpha 1$). Photostimulation: 1 s (magenta). While
1217 activation of MBON- $\alpha 1$ did not evoke detectable inhibition in the calcium signal, it
1218 effectively canceled the excitation by MBON- $\alpha 3$.
1219

1220 **Figure 4 – figure supplement 1. Excitatory interconnections between UpWiNs.**
1221 (A) Expression of Chrimson-tdTomato (red) and GCaMP6s (green) in UpWiNs. To
1222 express them in mutually exclusive subsets of UpWiNs, GCaMP expression was driven
1223 by a broad UpWiN driver 64A11-LexA, while Chrimson-tdTomato and LexAp65-DBD2-
1224 RNAi were driven in a subset of UpWiNs by SS67249. White box in the left image
1225 indicates an example axonal region of interest (ROI), which is zoomed in on the right
1226 image. Scale bar, 5 μm .
1227 (B) Thresholded images of GCaMP and Chrimson-tdTomato fluorescence. A small
1228 number of voxels that showed co-expression of GCaMP and Chrimson, presumably due
1229 to incomplete RNAi, were excluded from analysis.
1230 (C) Two-photon imaging of GCaMP6s signals (mean $\Delta F/F \pm SEM$; n = 8). 1-s
1231 photostimulation (magenta) evoked calcium responses in both axonal and dendritic
1232 ROIs.

1233 **Figure 5. Optogenetic appetitive conditioning enhances the response to the**
1234 **conditioned odor in UpWiNs.**
1235 (A) Optogenetic conditioning was performed by pairing photostimulation of PAM-DANs
1236 with odor presentation. Expression of ChrimsonR-mVenus was driven by 58E02-LexA,
1237 and in vivo whole-cell recordings were made from UpWINs labeled by GFP using
1238 SS67249-split-GAL4. 1-min presentation of OCT was paired with LED stimulation (1 ms,
1239 2 Hz, 120 times), followed by 1-min presentation of MCH alone.
1240 (B) Representative recording from a single fly. Gray bars indicate 1-s odor presentation.
1241 (C) Mean ($\pm SEM$) odor responses (n = 6). Spikes were removed by a low-pass filter.
1242 (D) Summary data of mean ($\pm SEM$) odor-evoked membrane depolarization. Gray lines
1243 indicate data from individual neurons. Responses to OCT were potentiated (p < 0.01;
1244 repeated-measures two-way ANOVA followed by Tukey's post hoc multiple comparisons
1245 test), while those to MCH did not change (p = 0.9).

1246 **Figure 5 – figure supplement 1. Expression patterns of SS67249**
1247 (A) Expression of CsChrimson-mVenus driven by SS67249.
1248 (B-D) MCFO image of neurons in SS67249 (red) and SMP353 (gray) with outline of the
1249 MB and the standard brain.

1250 **Figure 5 – figure supplement 2. Reciprocal experiment of optogenetic appetitive**
1251 **conditioning.**
1252 (A) Experimental design and protocol. Same as Figure 5 except that MCH was paired
1253 with DAN photostimulation.
1254 (B) Representative recording from a single fly. Gray bars indicate 1-s odor presentation.
1255 (C) Mean ($\pm SEM$) odor responses (n = 5). Spikes were removed by a low-pass filter.
1256 (D) Summary data of mean ($\pm SEM$) odor-evoked membrane depolarization. Gray lines
1257 indicate data from individual neurons. Responses to MCH were potentiated (p < 0.001;
1258 repeated-measures two-way ANOVA followed by Tukey's post hoc multiple comparisons
1259 test), while those to OCT did not change (p = 0.4).
1260

1262
1263 **Figure 6. Activity of UpWiNs bias turning direction**
1264 (A) Fed or 40-48 hours starved flies were compared to assess requirement of starved
1265 status for UpWiNs to promote upwind locomotion. n = 14 (fed) and 16 (starved); ***,
1266 p<0.001, Mann-Whitney test;
1267 (B) Upwind locomotion during the 10s activation of UpWiNs in the arena with various
1268 rates of airflow. n = 9-16; **, p<0.01; Dunn's multiple comparison tests compared to the
1269 zero flow condition.
1270 (C) Right side or both sides of aristae were ablated one-day prior to experiments to
1271 measure upwind response during UpWiN activation. n = 20 (intact) and 40 (unilateral
1272 and bilateral); ***, p<0.001; Dunn's multiple comparison tests compared to the intact
1273 control.
1274 (D) Behavioral kinematics of UpWiN activation. The trajectories of individual flies during
1275 first 1.5 s of 10-s LED period were grouped to initially facing downwind or upwind if
1276 cos(upwind angle) was above 0.5 or below -0.5, respectively.
1277 (E) Cumulative angle of turning and forward walking speed during the first 10 frames
1278 (333 ms) after the onset of LED plotted against initial angle to upwind smoothed with
1279 +/- 30-degree bin. The number of trajectories analyzed for (SS33917, SS33918,
1280 MB077B, Empty-split-GAL4) were (2492, 3362, 772, 1582), respectively. Only flies that
1281 were at least 3 mm away from the edge of the arena were analyzed.
1282 (F-G) The violin-plots of the cumulative angle of turn to the upwind orientation or forward
1283 walking speed during the first 10 frames (333 ms) of odor onset. Only flies that oriented -
1284 90 to -150 or +90 to 150 degrees to upwind at the odor onset were analyzed. n = 444,
1285 540, 231, 219 for SS33917, SS33918, MB077B, Empty-split-GAL4, respectively. **,
1286 p<0.01; ***, p<0.001; Dunn's multiple comparison for the selected pairs, following
1287 Kruskal-Wallis test. Thick and thin horizontal lines are mean and SEM in (A-C) and
1288 median and quartile ranges in (F-G), respectively.

1289
1290
1291 **Figure 6-figure supplement 1**
1292 The cosine of angle to upwind, angular speed and forward walking speed are separately
1293 plotted for flies oriented downwind or upwind at the odor onset. Only flies that were 3
1294 mm away from the edge of the arena were analyzed. The source data are identical to
1295 Figure 2.

1296
1297
1298 **Figure 7. UpWiNs are required for memory-driven upwind locomotion**
1299 (A) Upwind response to the odor associated with sugar in control genotypes and flies
1300 that express tetanus toxin (TNT) in UpWiNs.
1301 (B) Time course of upwind response.
1302 (C) Appetitive memories of control genotypes and flies expressing shibire (*Shi*) in
1303 UpWiNs were tested one-day after odor-sugar conditioning at restrictive or permissive
1304 temperature.
1305 (D) Time course of fly's preference to quadrants with red LED light by
1306 SS33917>CsChrimson (blue) or empty-split-GAL4>CsChrimson (gray). The preference
1307 to red LED quadrants during the last 5 s of two 30-s activation period was significantly
1308 higher for SS33917>CsChrimson flies (right).
1309 (E) The probability of returning to the location where LED stimulation was terminated
1310 were measured as in Figure 2, but without airflow. See Figure 7-figure supplement 1 for
1311 the time courses and other parameters. UpWiN drivers are shown together with
1312 SS49755 from the screen.

1313
1314 **Figure 7-figure supplement 1 UpWiN activation phenotypes without airflow**
1315 Time course of the five parameters shown in Figure 2-figure supplement 1 but in the
1316 absence of airflow. Lines and filled areas around lines are mean and SEM; CsChrimson-
1317 expressing flies (blue) and empty-split-GAL4 control (gray). The return probability was
1318 calculated within a 15-s time window. High return probability during LED ON period (10-
1319 20s) does not necessarily mean that flies returned during LED ON period. If a fly is at the
1320 position A when t=10s, to be counted as “returned”, it needs to move more than 10mm
1321 away from A and move back to the position less than 3mm distance from A by t=25s. In
1322 the case of sugar sensory neuron activation with Gr64f-GAL4, the peak of return
1323 probability is shifted toward a later time point because flies stop and extend proboscis
1324 during activation period.
1325
1326

1327 Source Data

1328 Figure 1D- Source data 1: The values used for Figure 1D
1329 Figure 1E- Source data 2: The values used for Figure 1E
1330 Figure 1F- Source data 3: The values used for Figure 1F
1331 Figure 1H- Source data 4: The values used for Figure 1H
1332 Figure 1I- Source data 5: The values used for Figure 1I
1333 Figure 1J- Source data 6: The values used for Figure 1J
1334 Figure 1K- Source data 7: The values used for Figure 1K
1335 Figure 1L- Source data 8: The values used for Figure 1L
1336 Figure1-figure supplement 1-Source data 1: The values used for Figure1-figure
1337 supplement 1
1338 Figure 2A - Source data 1: The values used for Figure 2A
1339 Figure 2B - Source data 2: The values used for Figure 2B
1340 Figure 2-figure supplement1 - Source data 1"
1341 Figure 4A - Source data 1: The values used for Figure 4A
1342 Figure 4B - Source data 2: The values used for Figure 4B
1343 Figure 4C - Source data 3: The values used for Figure 4C
1344 Figure 4 - figure supplement 1 -Source data 1"
1345 Figure 5 - figure supplement 2B -Source data 1: The values used for Figure 5 - figure
1346 supplement 2B
1347 Figure 5 - figure supplement 2C -Source data 2: The values used for Figure 5 - figure
1348 supplement 2C
1349 Figure 5 - figure supplement 2C -Source data 3: The values used for Figure 5 - figure
1350 supplement 2C
1351 Figure 5B - Source data 1: The values used for Figure 5B
1352 Figure 5C - Source data 2: The values used for Figure 5C
1353 Figure 5D - Source data 3: The values used for Figure 5D
1354 Figure 6A- Source data 1: The values used for Figure 6A
1355 Figure 6B- Source data 2: The values used for Figure 6B
1356 Figure 6C- Source data 3: The values used for Figure 6C
1357 Figure 6D- Source data 4: The values used for Figure 6D
1358 Figure 6E- Source data 5: The values used for Figure 6E
1359 Figure 6F- Source data 6: The values used for Figure 6F
1360 Figure 6G- Source data 7: The values used for Figure 6G
1361 Figure 6 - figure supplement 1 - Source data 1: The values used for Figure 6 - figure
1362 supplement 1
1363 Figure 7A- Source data 1: The values used for Figure 7A

1364 Figure 7B- Source data 2: The values used for Figure 7B
1365 Figure 7C- Source data 3: The values used for Figure 7C
1366 Figure 7D- Source data 4: The values used for Figure 7D
1367 Figure 7E- Source data 5: The values used for Figure 7E
1368 Figure 7 - figure supplement 1 - Source data 1: The values used for Figure 7 - figure
1369 supplement 1
1370

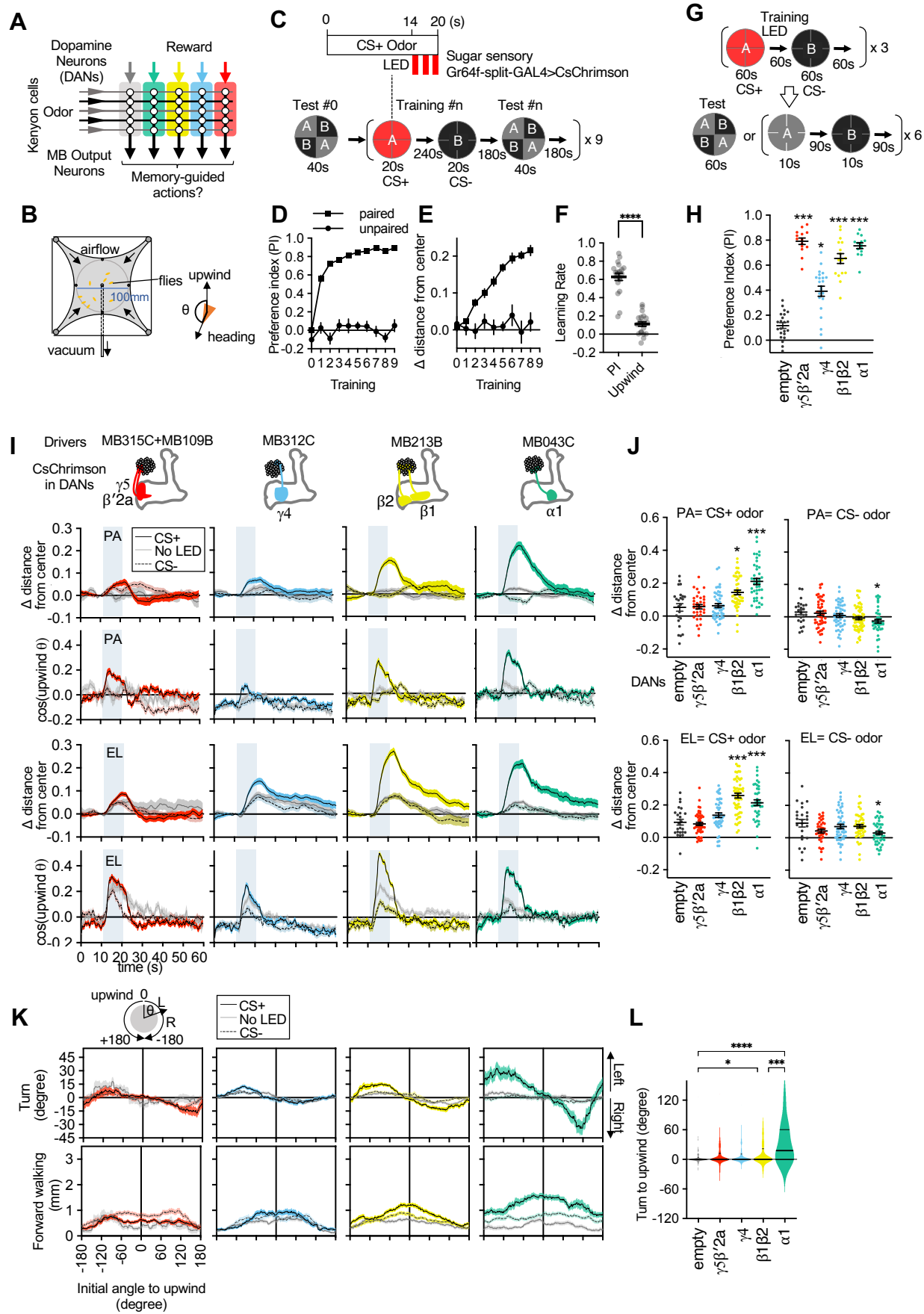


Figure 1

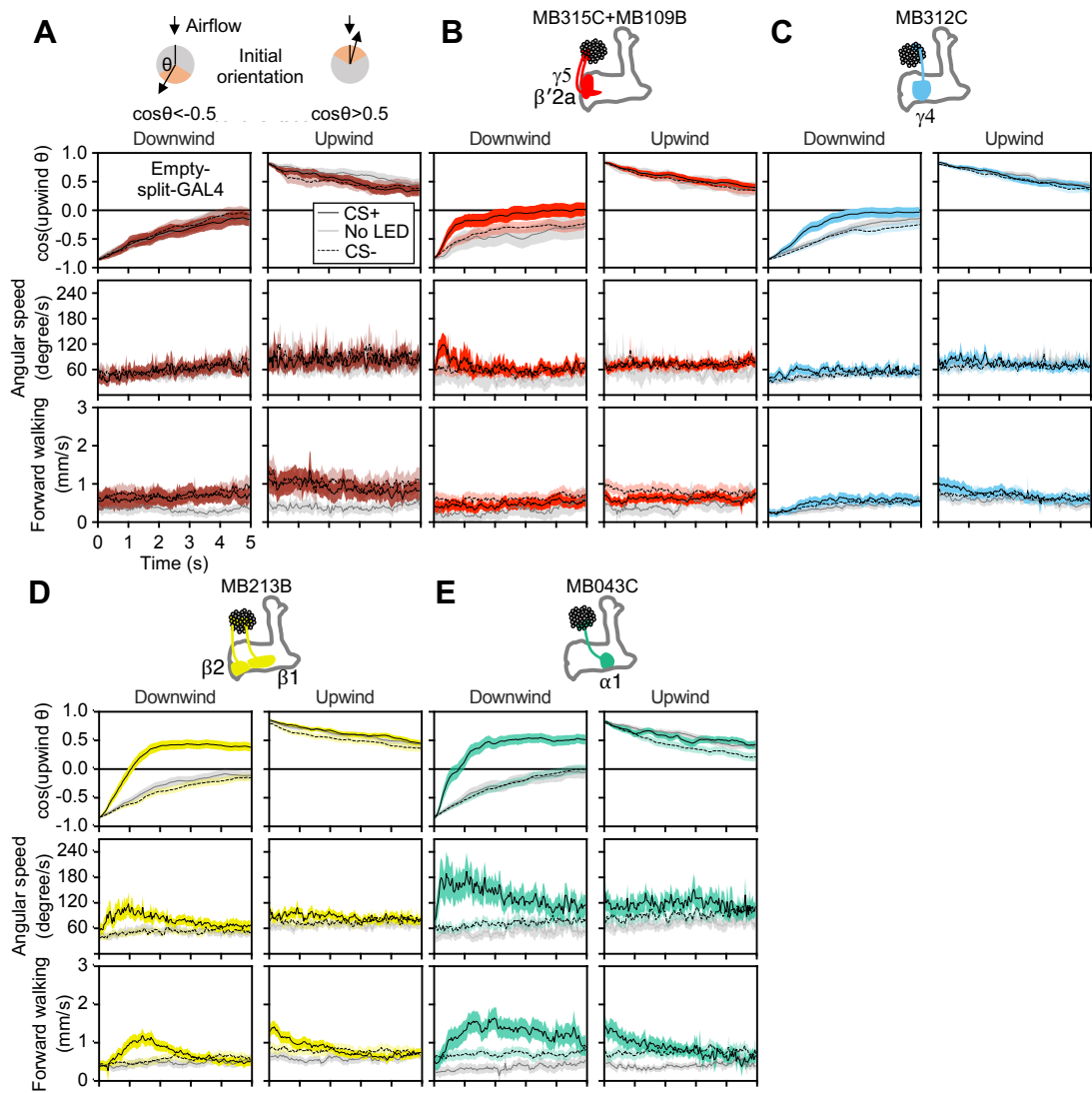


Figure 1-figure supplement 1

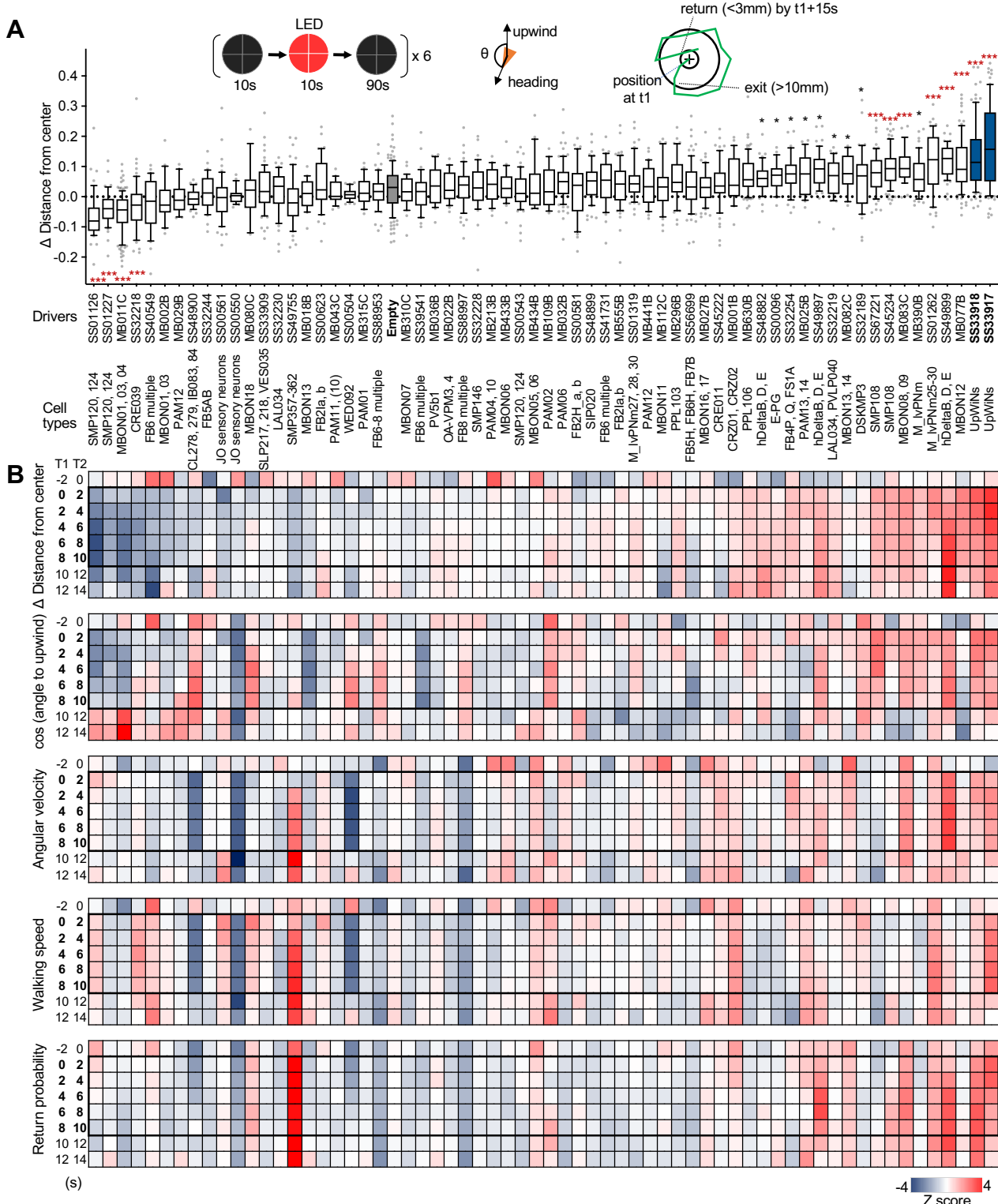


Figure 2

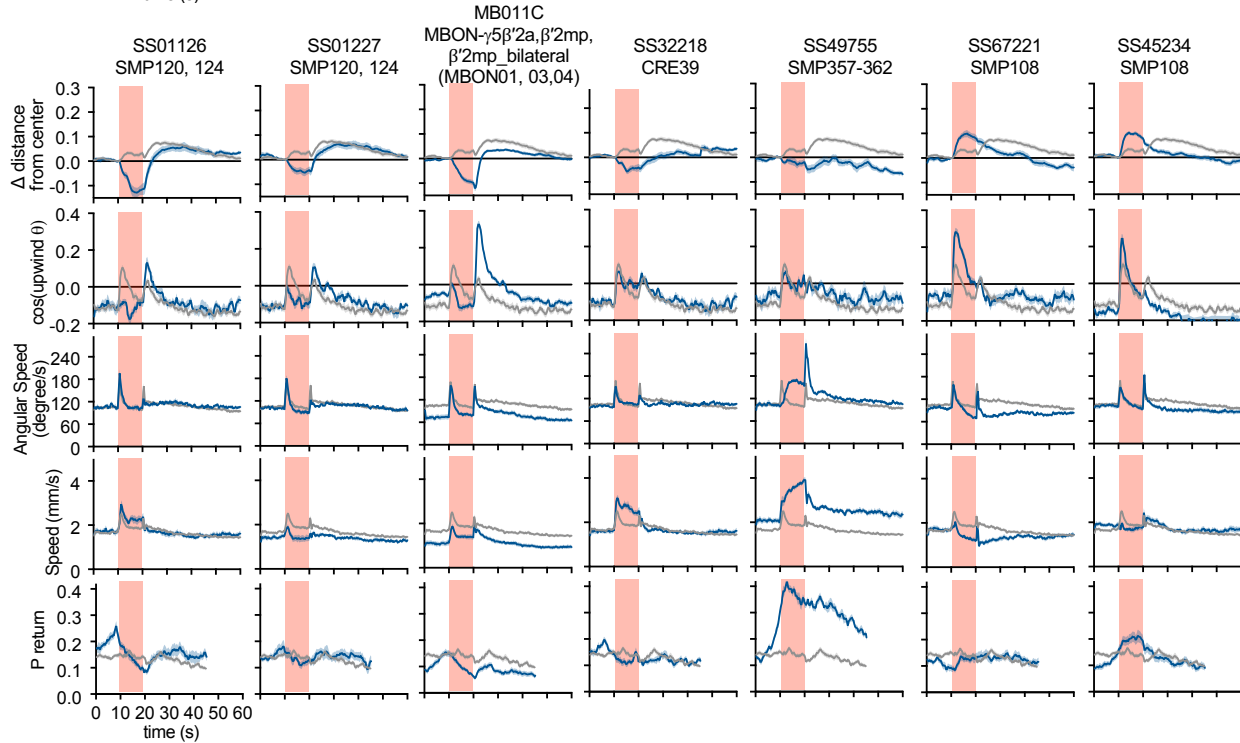
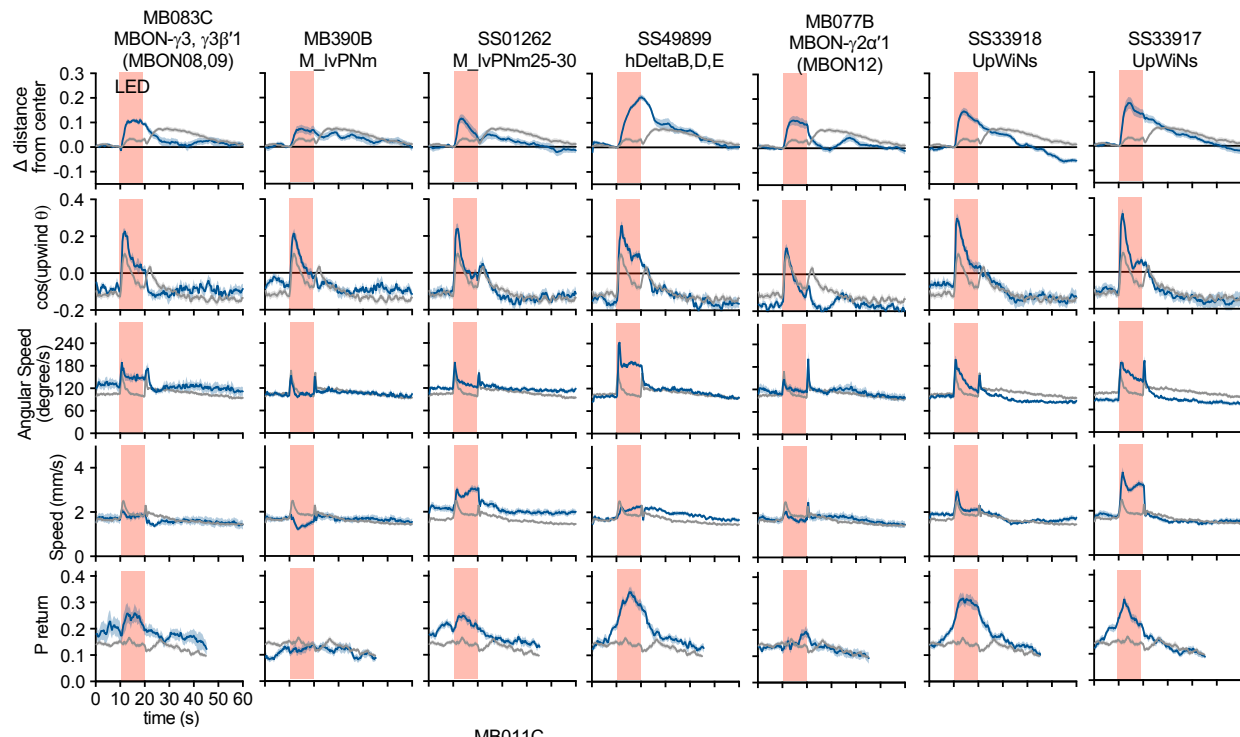
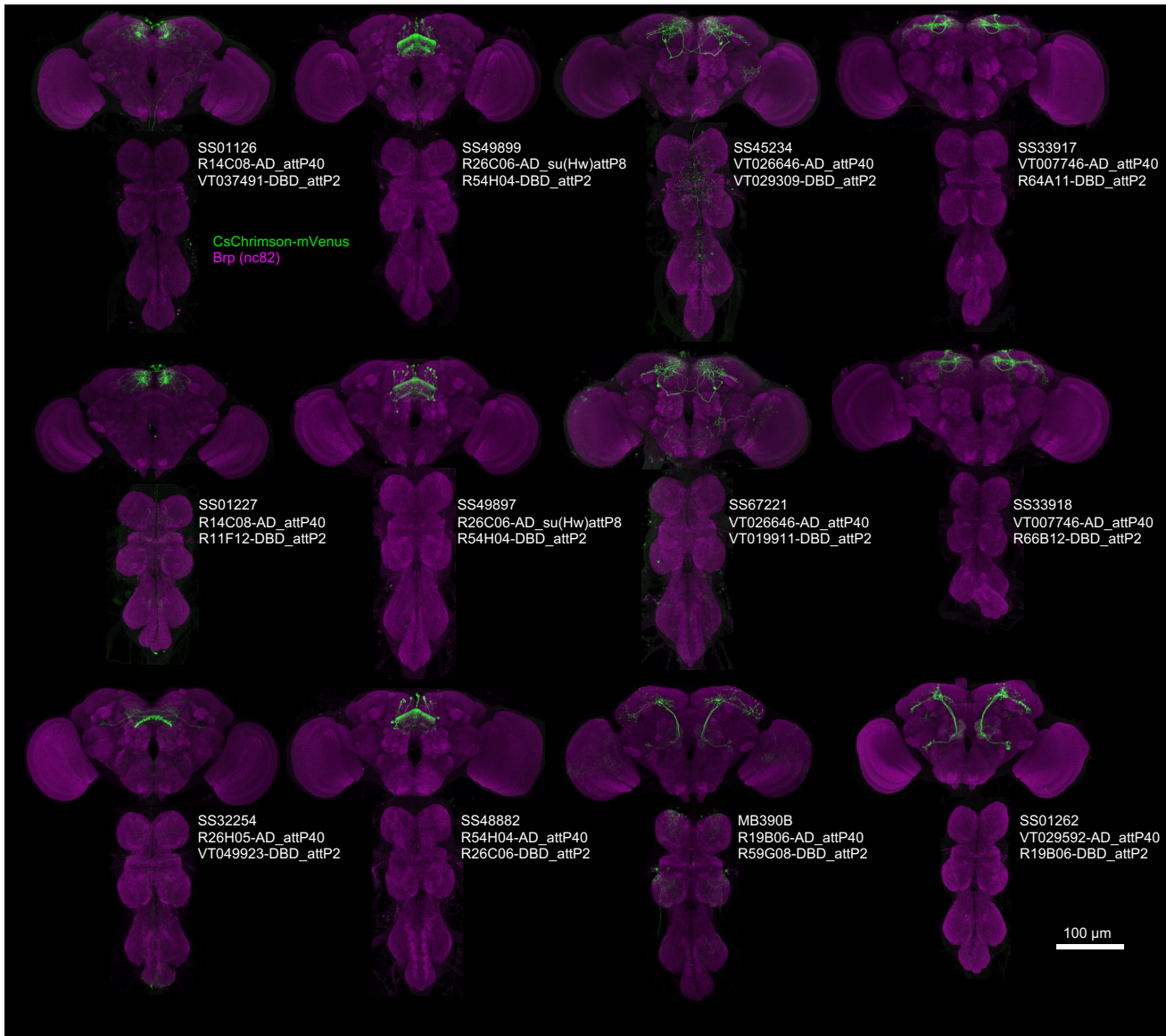


Figure 2-figure Supplement 1



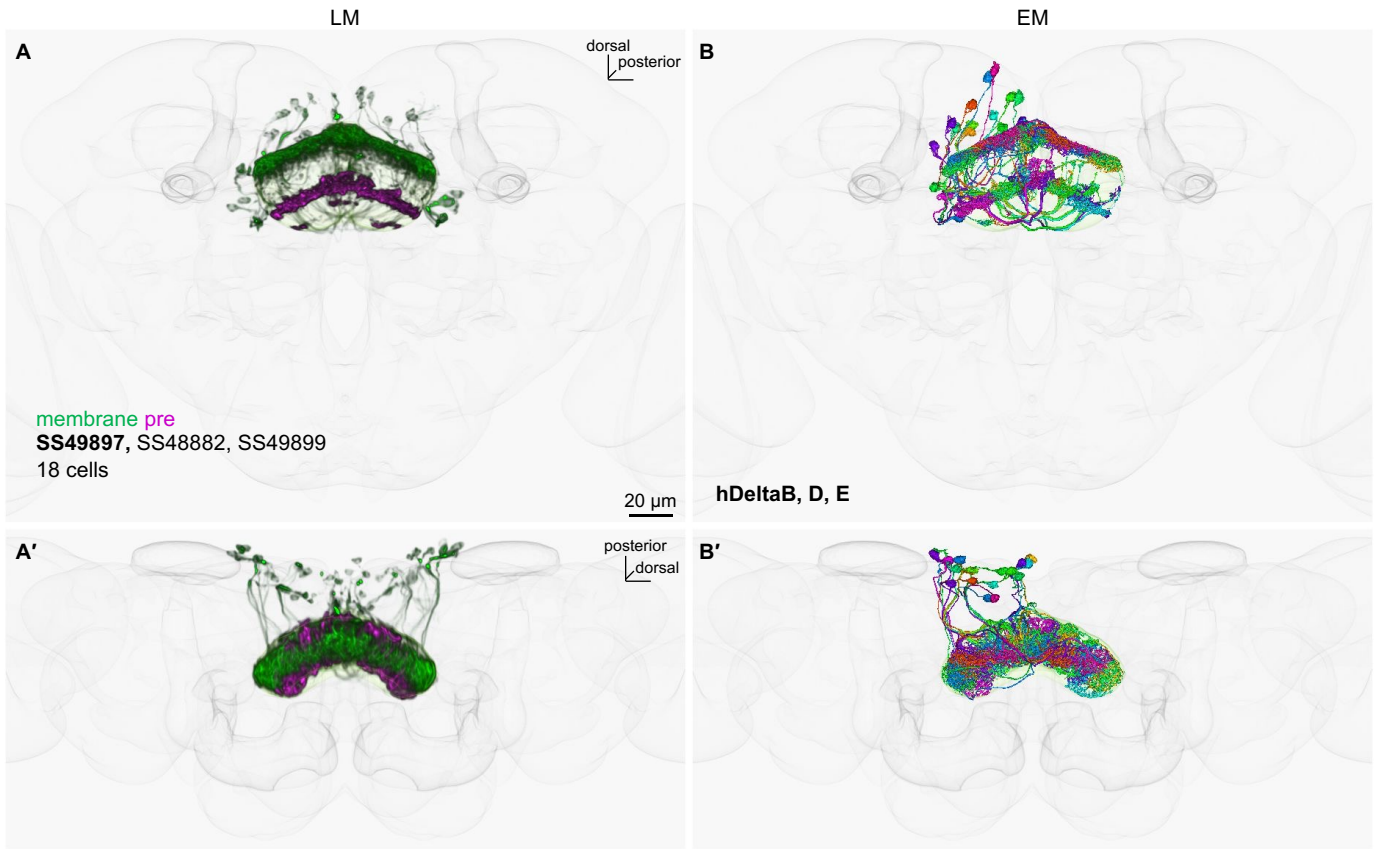


Figure 2-figure Supplement 3

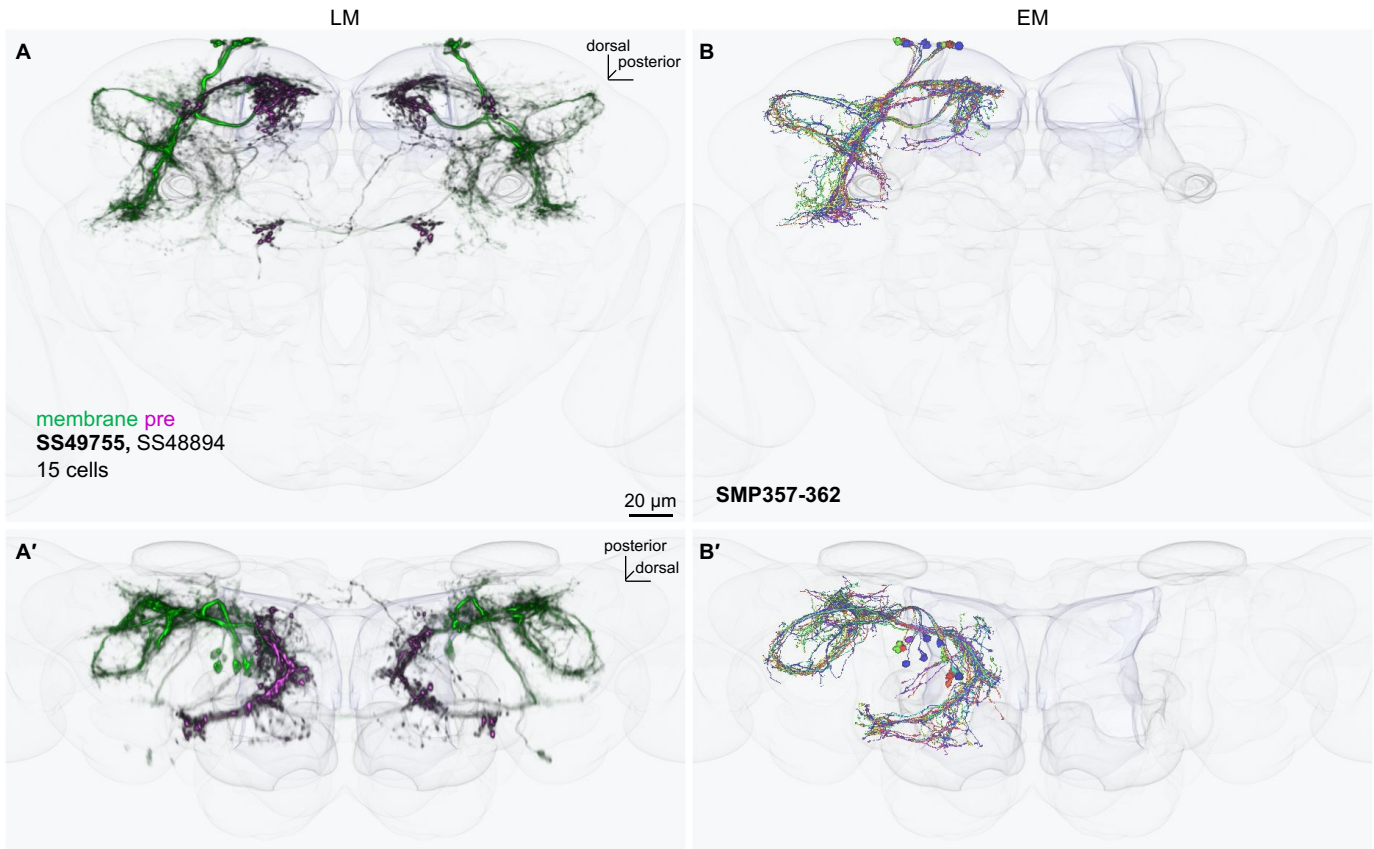


Figure 2-figure Supplement 4

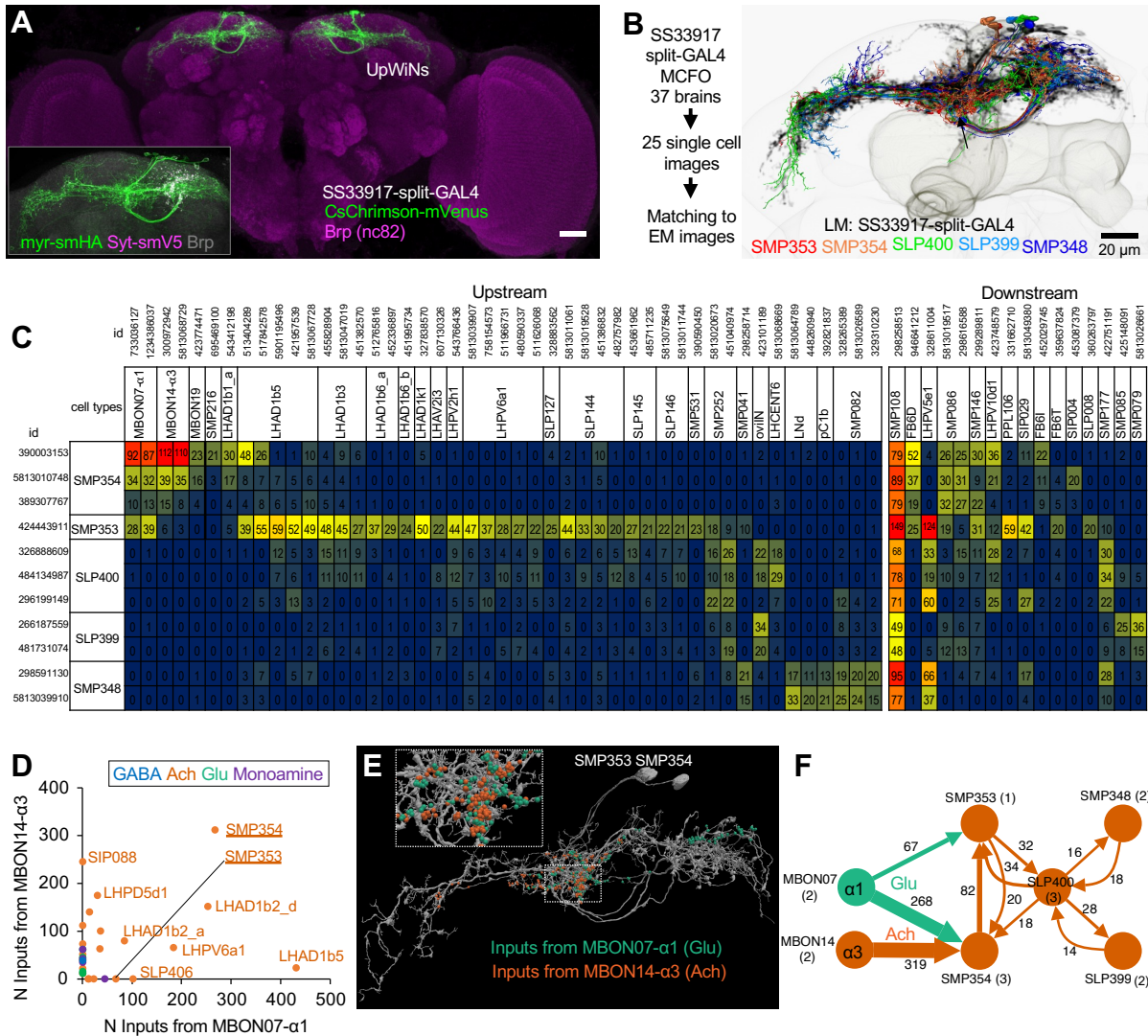


Figure 3

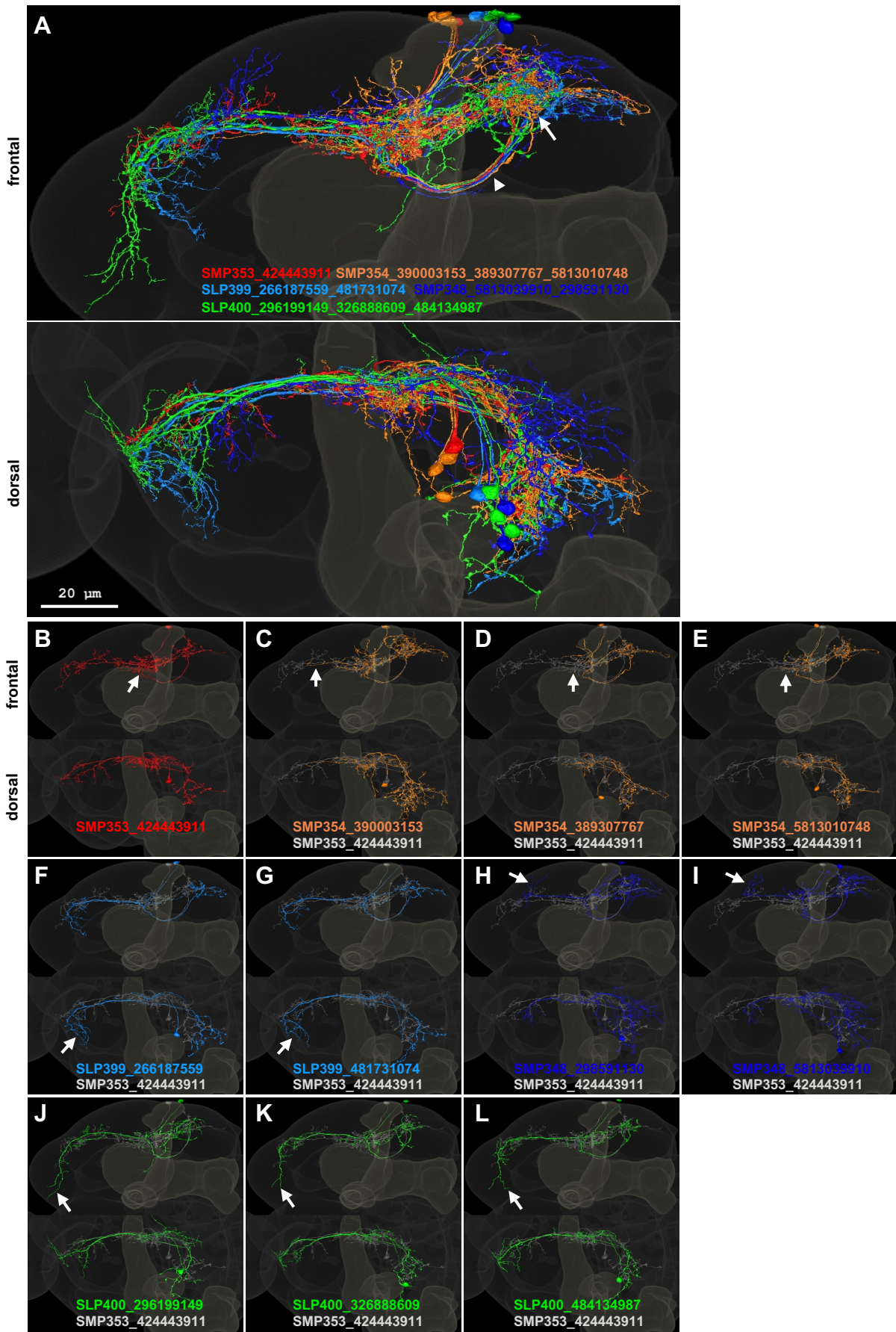


Figure 3-figure supplement 1

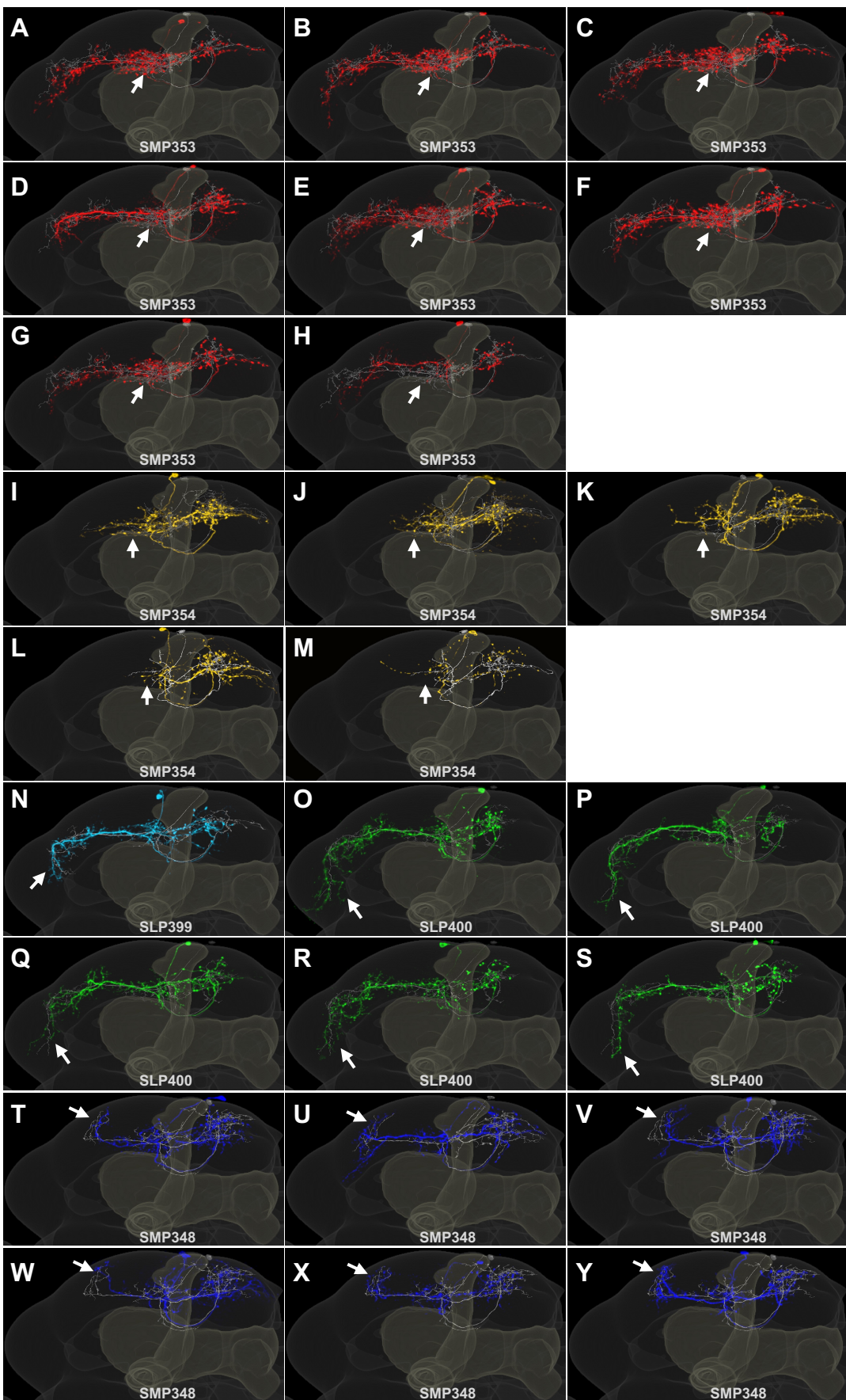


Figure 3-figure supplement 2

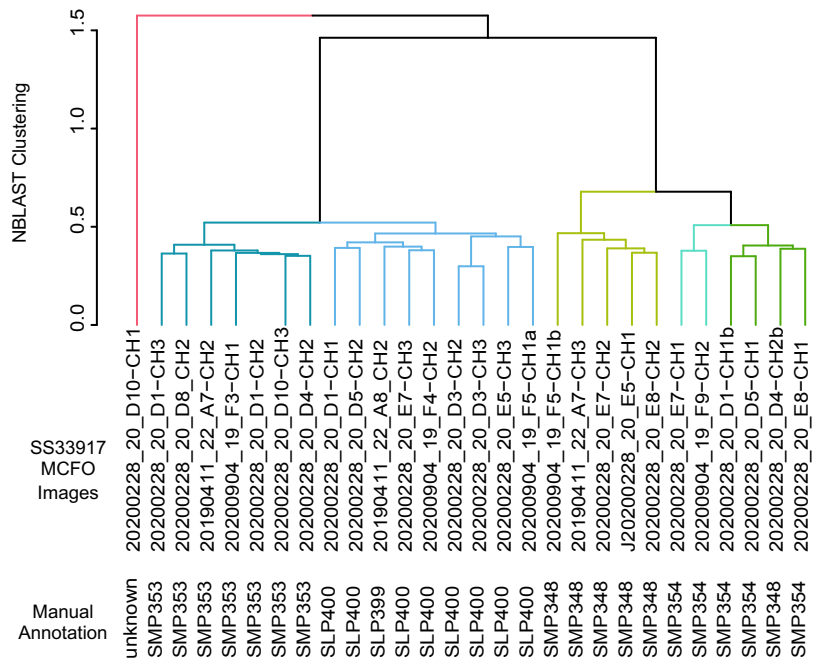
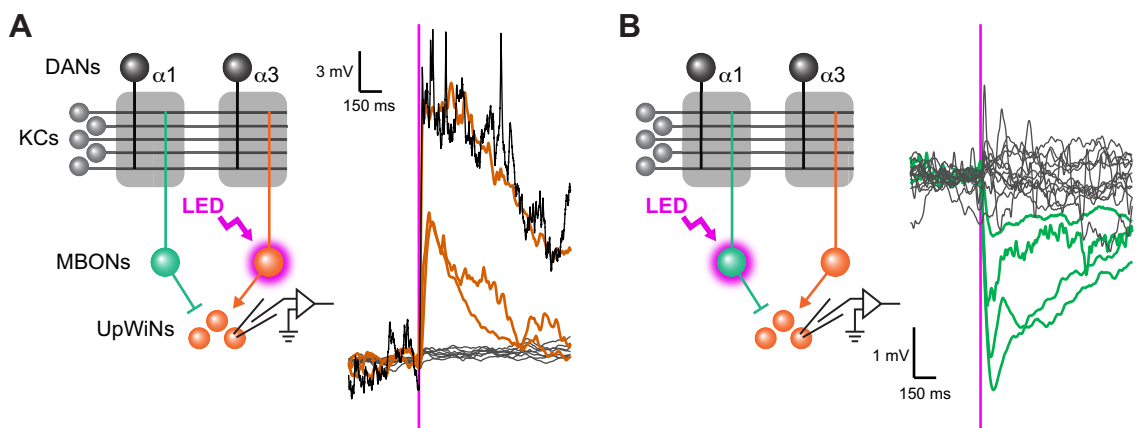


Figure 3-figure supplement 3

Cell type		MB compartments																				
Cell type	Transmitter	Glu	Ach	Glu	Ach	Glu	(GABA)	Glu	GABA	Glu	Ach	Glu	GABA									
LHAD1b5	ACh	431	23	0	0	0	0	0	0	0	0	0	0	0	0	0	0	0	0	0	0	0
SMP354	ACh	268	311	0	0	0	0	0	0	0	0	0	0	0	0	0	0	0	0	0	0	0
LHAD1b2_d	ACh	253	152	258	59	53	13	0	0	10	0	0	0	0	0	0	0	0	0	0	0	0
LHPV6a1	ACh	183	66	0	0	0	0	0	0	0	0	0	0	0	0	0	0	0	0	0	0	0
SLP406	ACh	102	0	0	0	0	0	0	0	0	0	0	0	0	0	0	0	0	0	0	0	0
LHAD1b2_a	ACh	84	79	240	62	47	0	0	0	11	0	0	0	0	0	0	0	0	0	0	0	0
SMP353	ACh	67	0	0	0	0	0	0	0	0	0	0	0	0	0	0	0	0	0	0	0	0
PPM1201	DA	45	0	0	0	0	0	317	0	0	0	0	0	0	0	0	0	0	0	0	0	0
SMP031	ACh	36	100	206	106	0	51	0	0	165	28	0	0	0	0	0	32	0	0	10	0	0
LHAD1k1	ACh	35	63	0	0	0	0	0	0	0	0	0	0	0	0	0	0	0	0	0	0	0
LHPD5d1	ACh	36	174	231	53	0	41	0	0	0	86	0	0	43	0	0	11	11	0	0	0	0
LHAD1b6_a	ACh	23	0	11	0	0	0	0	0	0	0	0	0	0	0	0	0	0	0	0	0	0
LHAD1b3	ACh	14	140	0	0	0	0	0	0	0	0	0	0	0	0	0	0	0	0	0	0	0
LHAD1b2_c	ACh	13	0	40	11	40	0	0	0	0	0	0	0	0	0	0	0	0	0	0	0	0
LHAD1b2_b	ACh	12	0	0	0	0	0	0	0	0	0	0	0	0	0	0	0	0	0	0	0	0
SIP088	ACh	0	245	0	0	23	193	0	54	0	18	0	0	0	0	0	0	0	0	0	0	0
LHPV2h1	ACh	0	112	0	0	0	0	0	0	0	0	0	0	0	0	0	0	0	0	0	0	0
SMP549	ACh	0	73	0	12	0	0	0	0	0	18	0	0	0	0	0	0	0	0	0	0	0
SIP016	Glu	0	62	0	53	114	0	0	0	0	0	0	50	0	0	10	0	0	0	0	0	0
5-HT	HTMPDP01	0	61	0	0	10	0	0	15	0	0	0	0	0	0	0	0	0	0	0	0	0
SLP391	ACh	0	51	0	0	0	0	0	0	0	58	0	0	0	0	0	0	0	0	0	0	0
SIP015	Glu	0	45	0	128	169	0	0	0	0	0	0	0	0	0	0	0	0	0	0	0	0
SLP129_b	DA	0	42	0	0	0	0	0	0	0	0	0	0	0	0	0	0	0	0	0	0	0
SMP026	ACh	0	40	0	0	0	0	0	0	0	0	0	0	0	0	0	0	0	0	0	0	0
LHCENT9	GABA	0	38	33	0	0	96	0	145	0	48	0	16	0	11	0	25	0	0	0	0	0
SLP129_a	DA	0	35	0	0	0	0	0	0	0	0	0	0	0	0	0	0	0	0	0	0	0
LHAV6a9	ACh	0	22	0	0	0	0	0	0	0	0	0	21	0	0	0	0	0	0	0	0	0
SMP170	Glu	0	15	0	0	0	0	0	0	0	0	0	0	0	0	0	0	0	0	0	0	0
SMP194	ACh	0	11	0	23	0	0	0	0	0	0	0	0	12	0	0	0	0	0	0	0	0
SLP176	Glu	0	11	0	0	0	0	0	0	0	0	0	0	0	0	0	0	0	0	0	0	0

Figure 3 – figure supplement 4



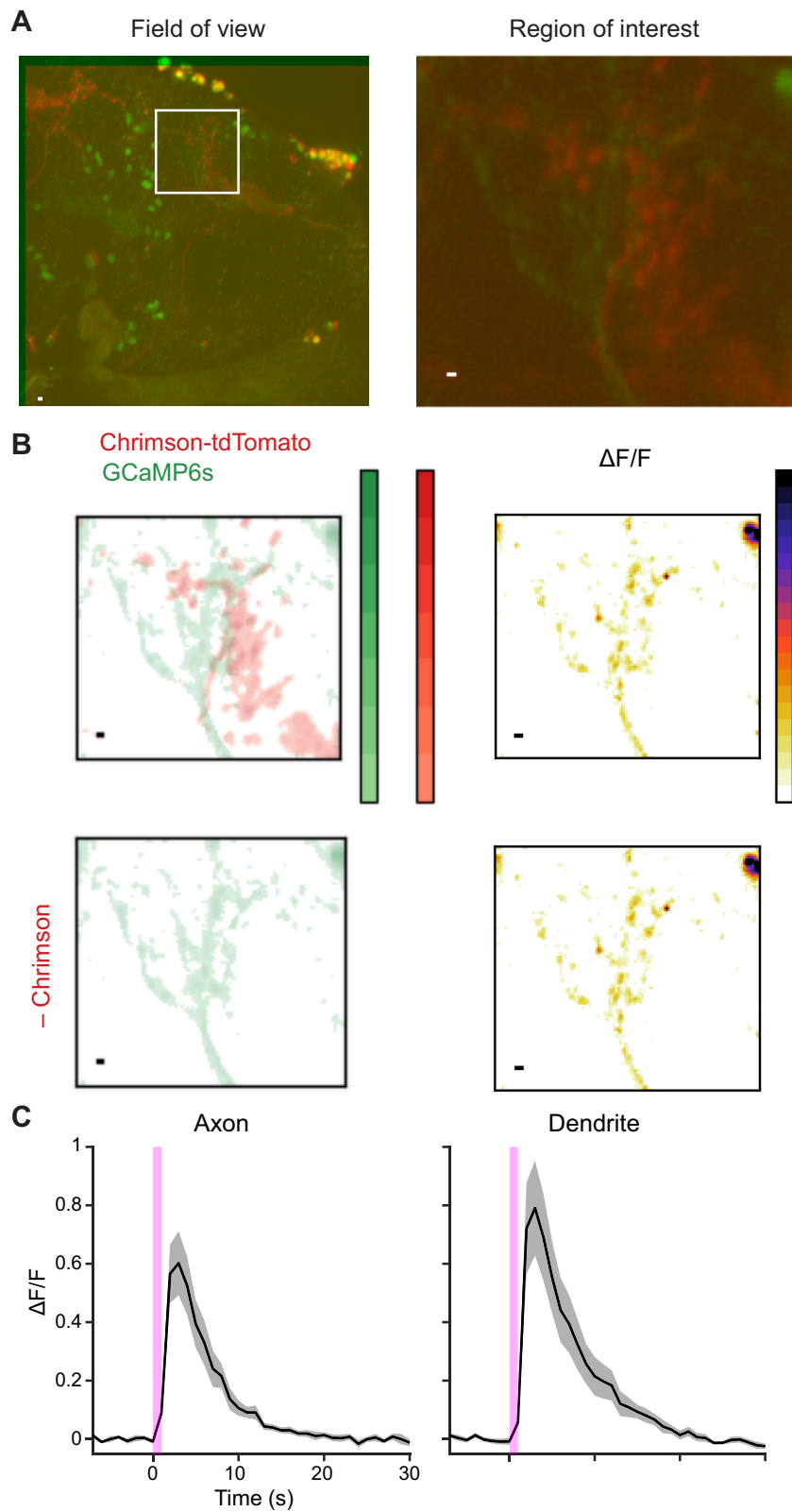
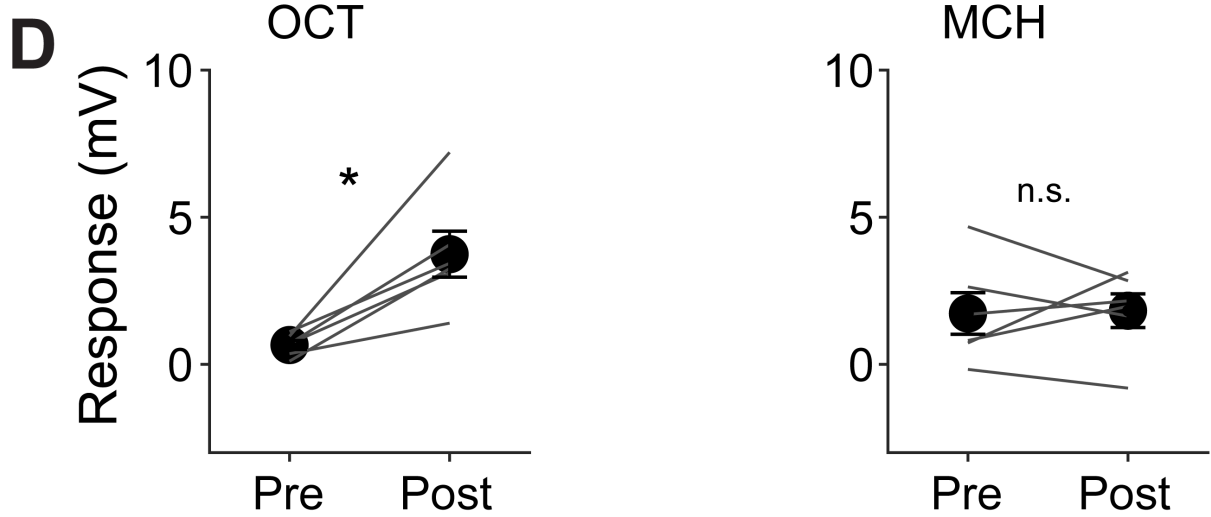
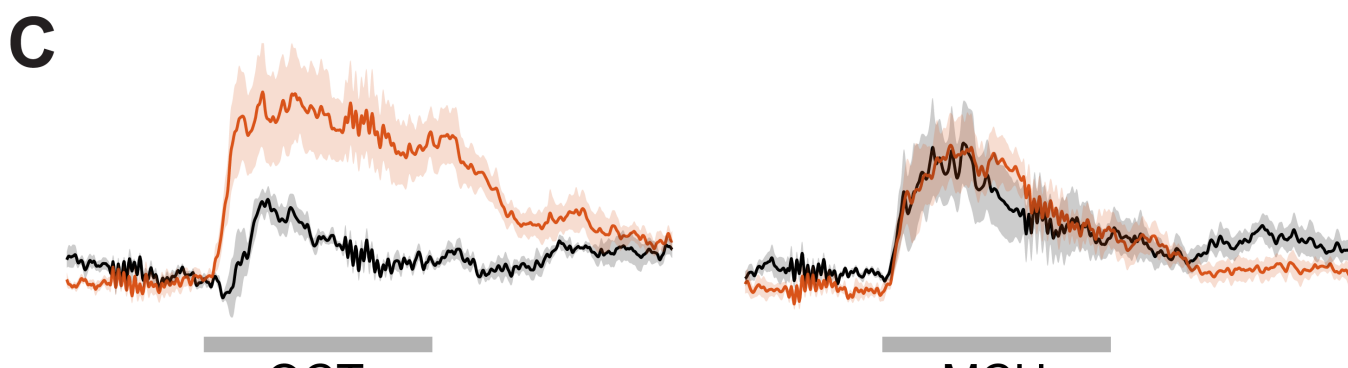
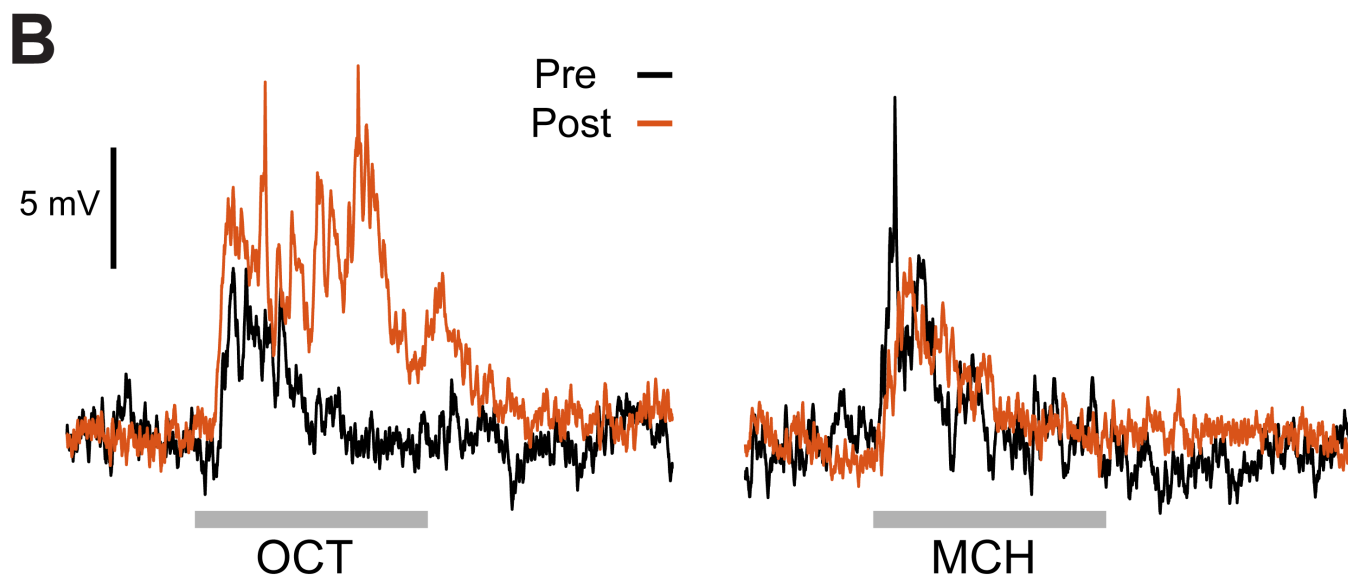
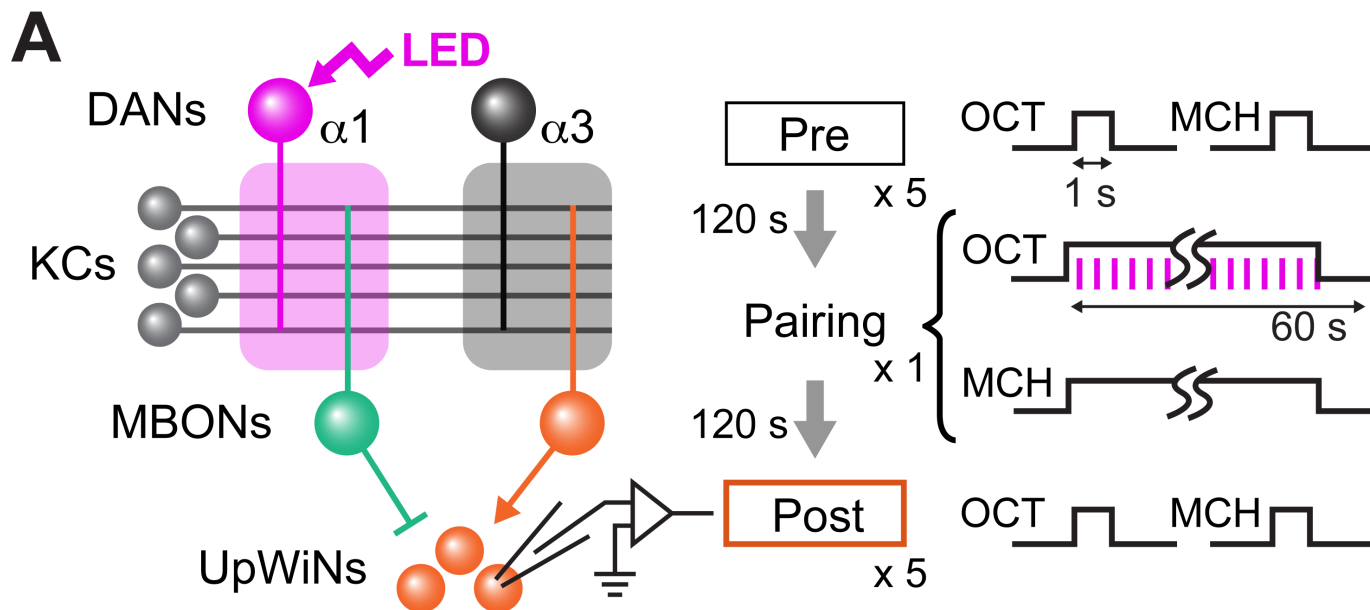


Figure 4-figure supplement 1



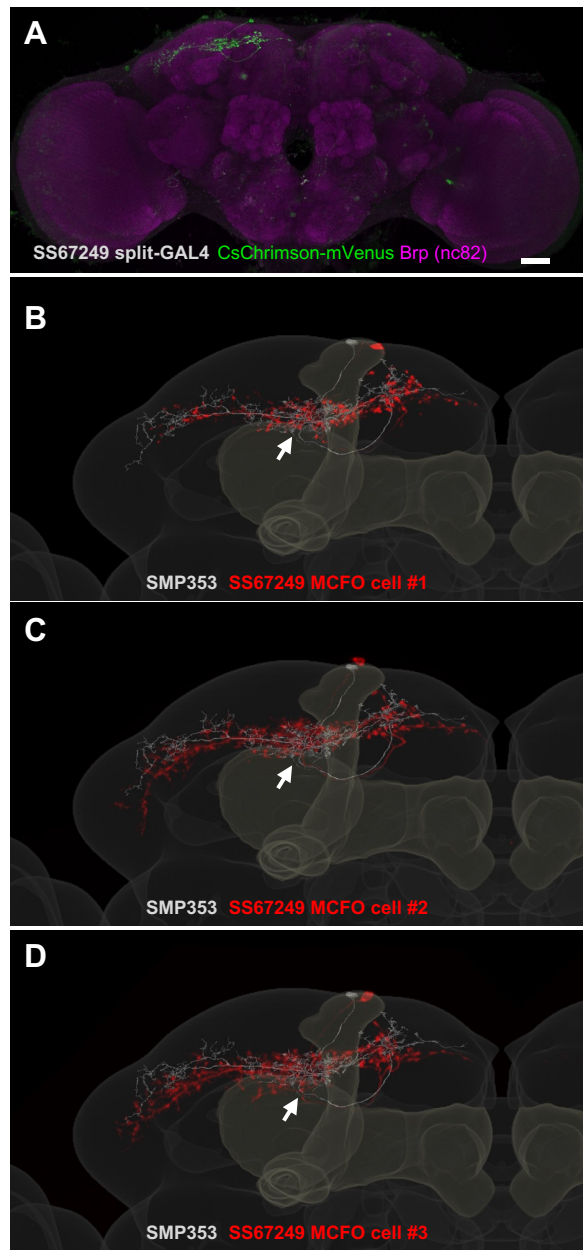
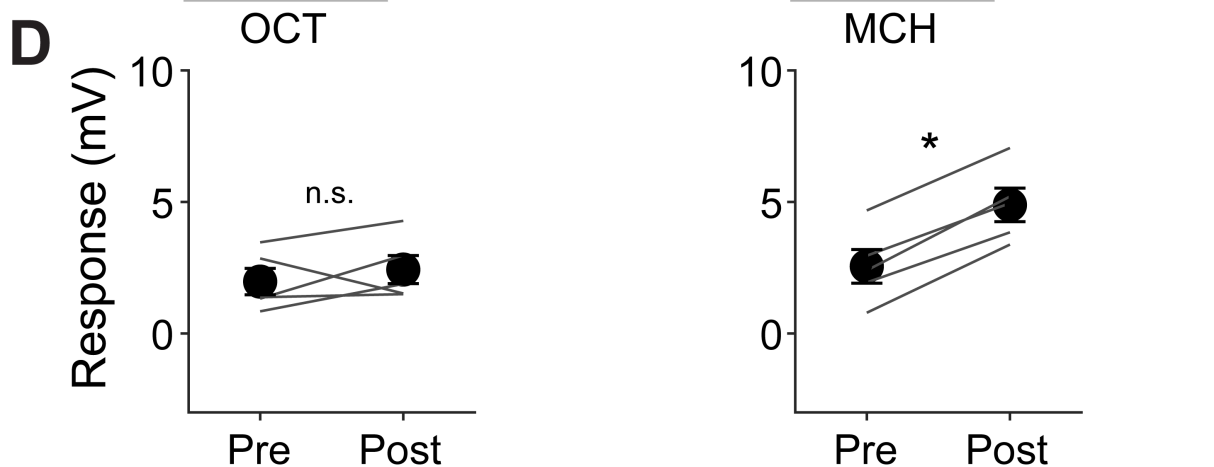
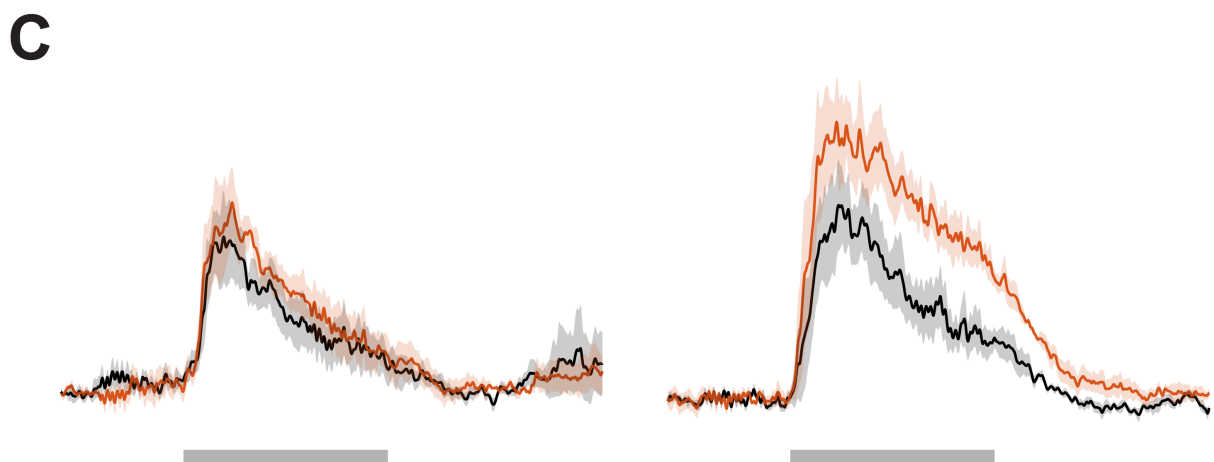
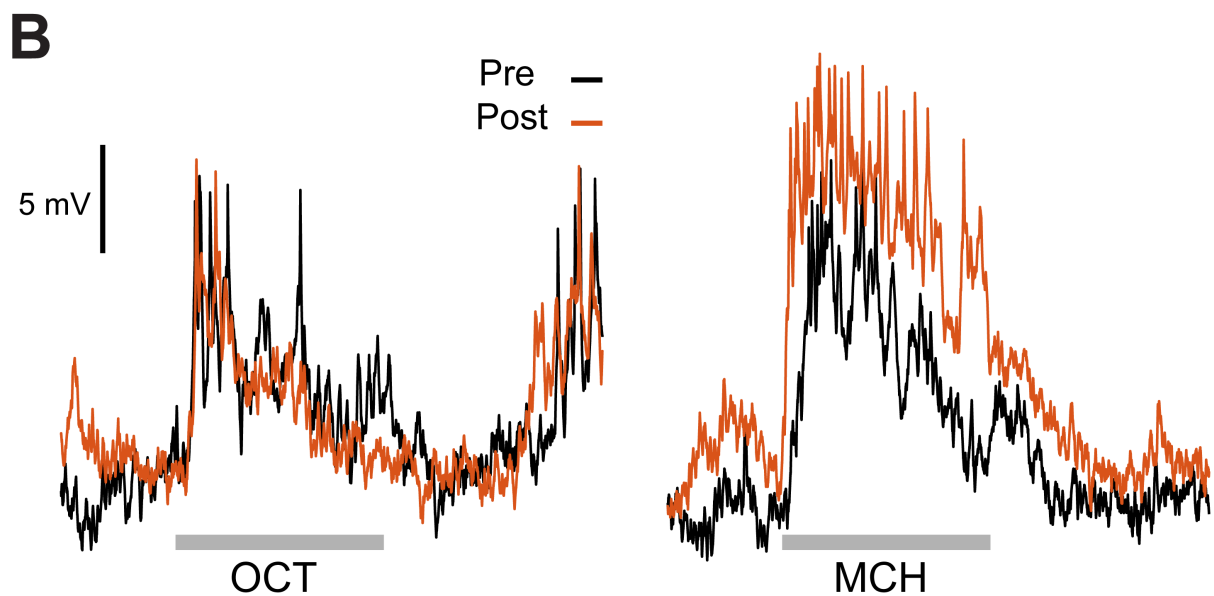
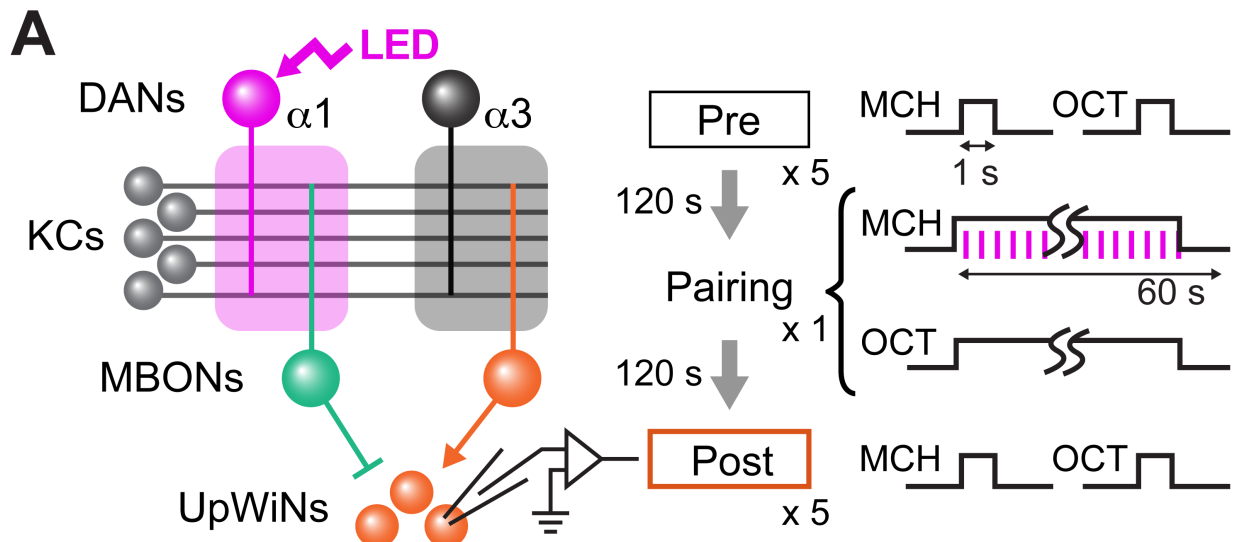


Figure 5 – figure supplement 1



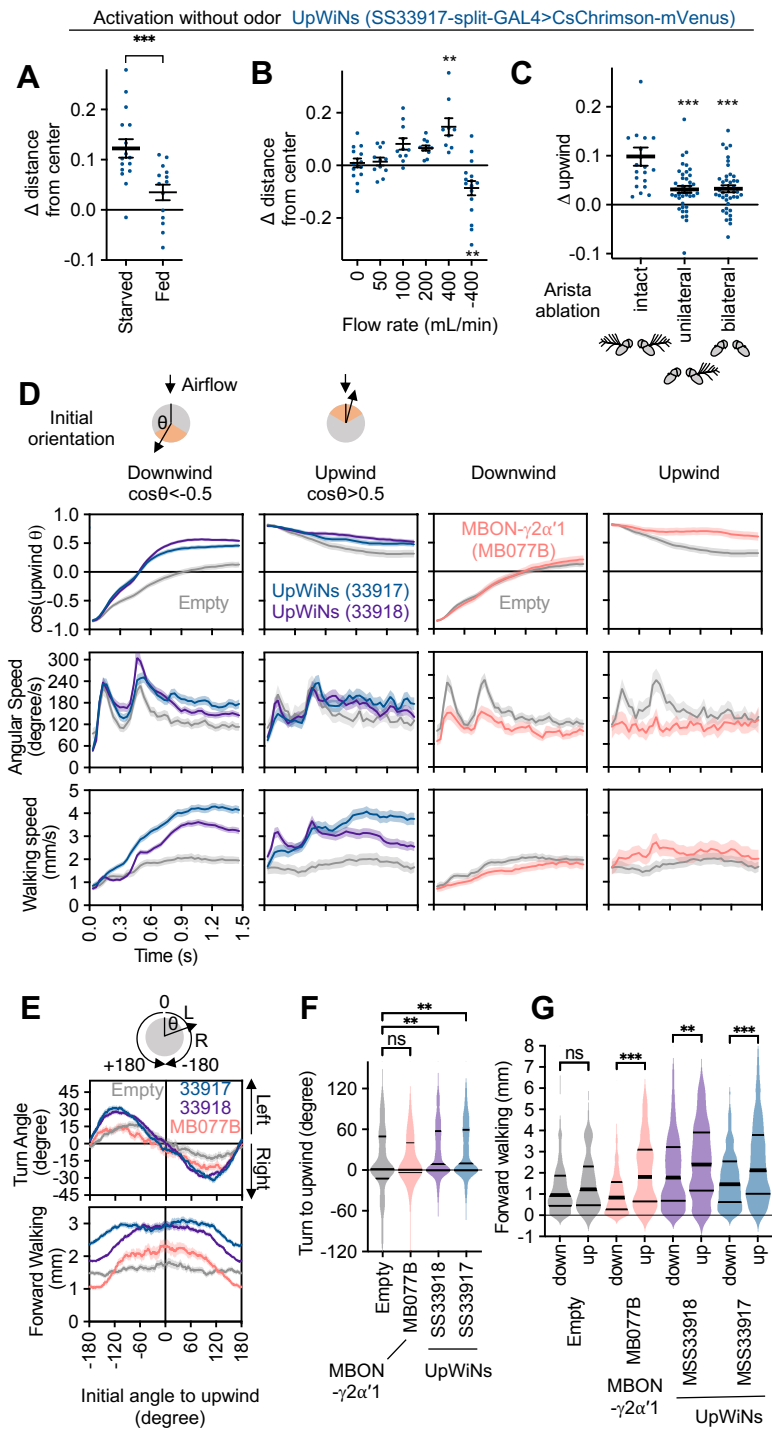


Figure 6

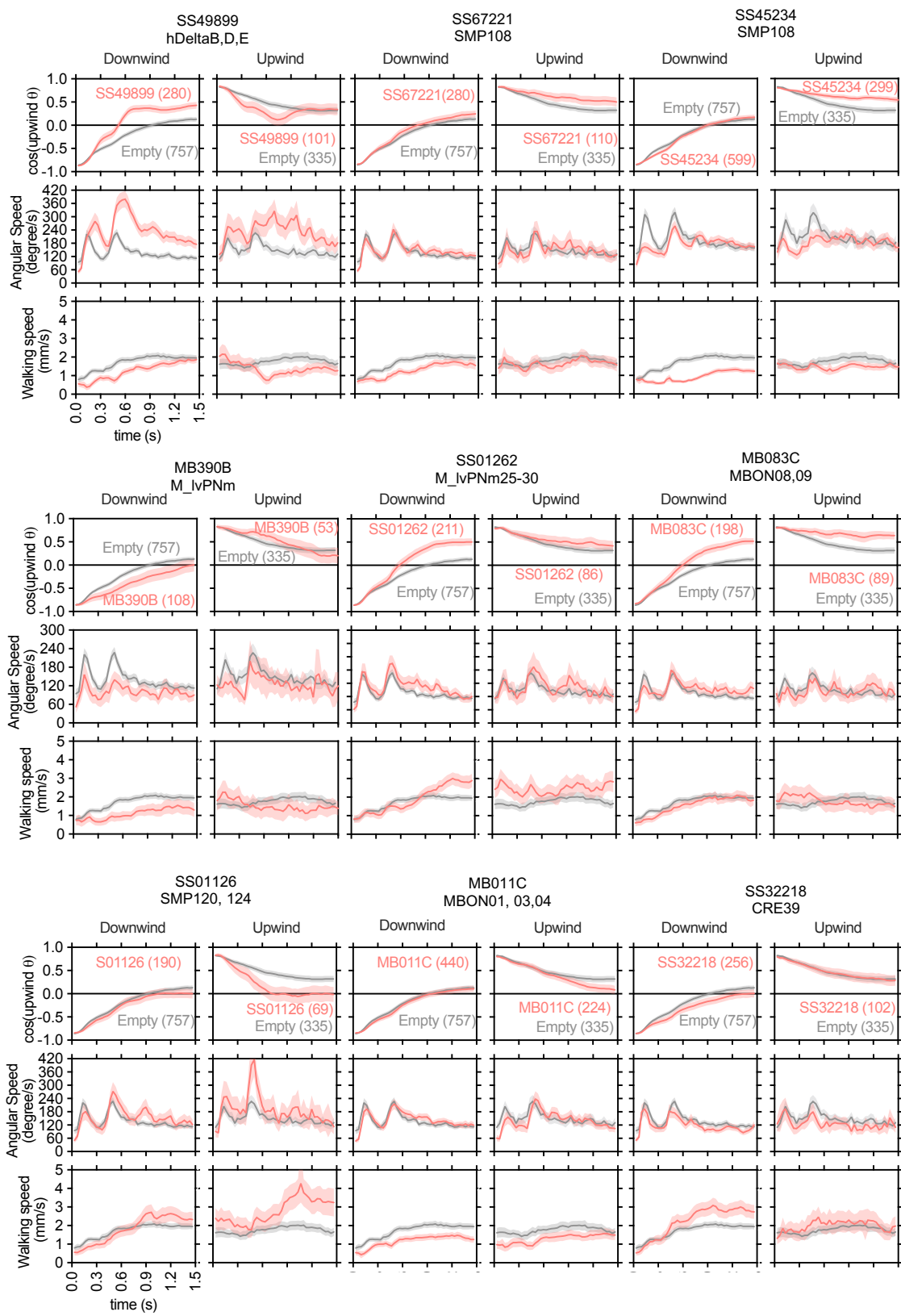


Figure 6-figure Supplement 1

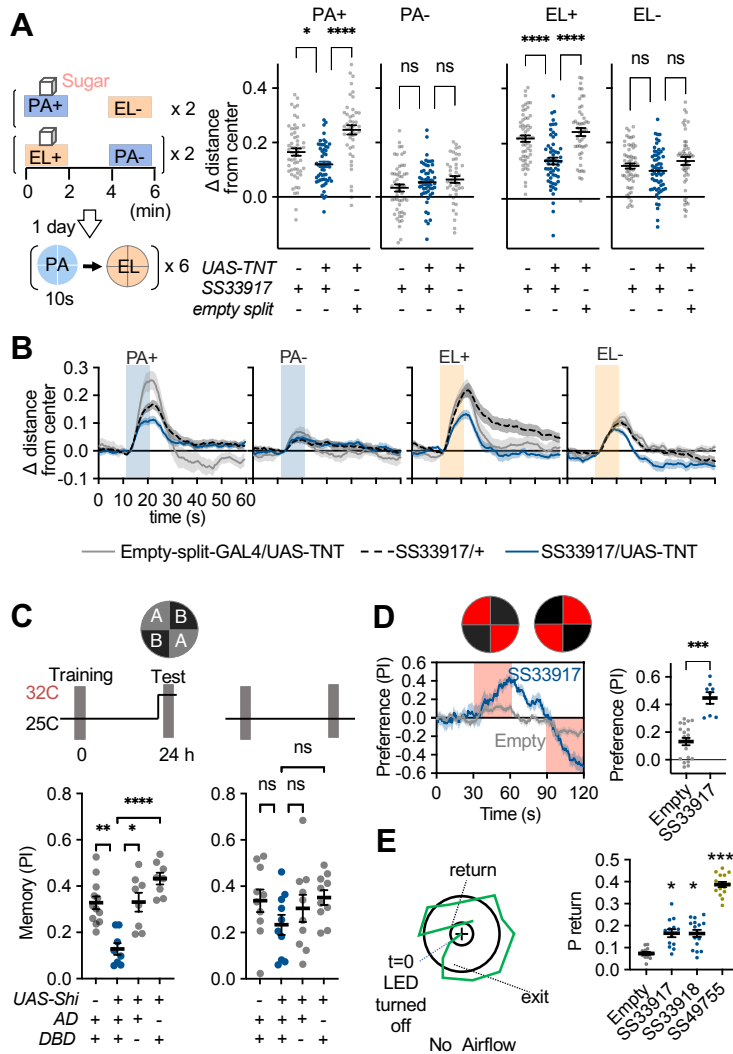


Figure 7

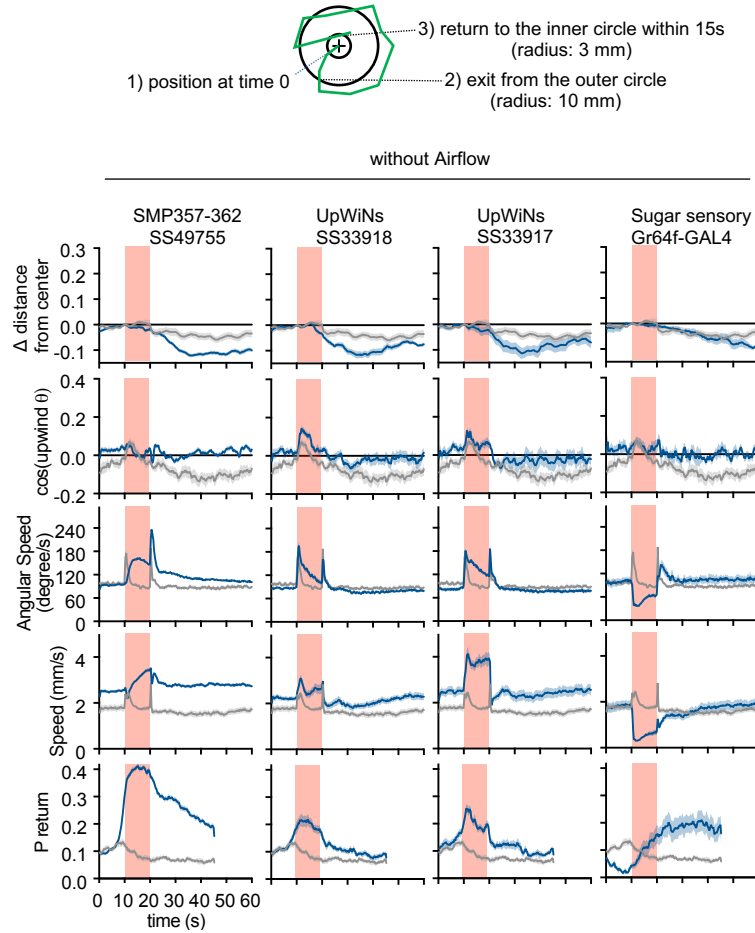


Figure 7-figure supplement 1